Kinetic and Thermodynamic Factors Influencing Palladium Nanoparticle Redispersion into Mononuclear Pd(II) Cations in Zeolite Supports

Trevor M. Lardinois,^{1,†} Keka Mandal,^{2,†} Vamakshi Yadav,³ Asanka Wijerathne,² Brandon K. Bolton,¹ Harrison Lippie,¹ Christina W. Li,³ Christopher Paolucci*,² Rajamani Gounder*,¹

ABSTRACT: Palladium cations and nanoparticles supported on oxides and zeolites are used as catalysts and adsorbents for a wide range of chemical reactions of practical importance, with various and distinct active site requirements. Consequently, sintering and redispersion processes that interconvert site-isolated Pd cations and agglomerated nanoparticles underpin catalyst activation and deactivation phenomena, yet the influence of Pd nanoparticle size distribution and gas conditions on the thermodynamic and kinetic factors influencing such interconversion are imprecisely understood. Here, we prepare Pd nanoparticles of different particle size and distribution (normal, log-normal) supported on high-symmetry crystalline zeolites to access well-defined materials whose Pd site distributions can be quantitatively characterized by experiment and modeled accurately by theory. *Ab initio* thermodynamic modeling and isothermal (593–973 K) wet and dry air treatments of Pd-zeolites reveal that the widely observed deactivation under low-temperature hydrous environments reflect site interconversion thermodynamics that favor the agglomeration of isolated Pd cations into nanoparticles. Under high-temperature anhydrous conditions, experimental kinetic measurements and kinetic Monte Carlo simulations evince the preeminence of kinetic factors on Pd nanoparticle redispersion into cations, which proceeds at rates that are strongly influenced by the initial Pd particle size distribution and via a substrate diffusion-mediated Ostwald ripening process whereby Pd monomers are captured in an atom trapping process at anionic exchange sites (framework Al) in the zeolite support. These findings resolve longstanding questions regarding the roles of H₂O and support interactions in Pd redispersion processes and identify strategies to enhance or suppress Pd site interconversion by modifying oxide supports and gas conditions.

1. INTRODUCTION

The dynamic processes responsible for the sintering of metal nanoparticles and their redispersion into smaller clusters and isolated atoms and ions on oxide supports strongly influence the reactivity, selectivity, deactivation, and regeneration of heterogeneous catalysts and adsorbent materials. 1-6 The redispersion of nanoparticles and clusters to single atoms results in catalyst deactivation for methane oxidation on Pd supported on Al₂O₃⁷ and Pt supported on CeO₂, 8 NO reduction in the presence of CO on Pt supported on aluminosilicate MWW zeolites, 9,10 CO oxidation on various metals (Ru, 11 Rh, 11 Ir, 11 Pt, 12 and Pd 13) supported on CeO₂, and propane dehydrogenation on Pt-Sn clusters supported on CeO₂. 14 Conversely, the formation of metal nanoparticles from single atoms causes deactivation of Pt, 8,15 Pd, 11,15 Cu, 16 and Rh15 on CeO₂ for CO oxidation, Au on CeZrO₄17 and CeO₂¹⁸ for the water-gas shift reaction, Au on carbon for acetylene hydrochlorination, 19,20 and Rh on aluminosilicate zeolites or TiO₂ for methane oxidation to methanol.²¹ Compared to catalvsts containing larger nanoparticles, catalvsts composed of single atoms and sub-nanometer sized clusters are typically more susceptible to structural changes in response to their reaction environment, and thus tend to sinter more readily via Ostwald ripening (OR) under reducing conditions at high

temperatures.^{1,22} Redispersion of nanoparticles to single atoms and ions can facilitate catalyst regeneration;^{23,24} however, the atomistic details of the thermodynamic driving forces and kinetic mechanisms governing such redispersion processes are not well-understood.

The structural interconversion between oxide-supported Pd nanoparticles and cations is strongly affected by reaction conditions and nanoparticle sizes, 7,10,25-32 and is of particular relevance for several catalytic and adsorption applications including CO oxidation, 11,13,15,33-35 Wacker oxidation, 36-38 methane oxidation, 39-43 alkene hydrogenation, 44-47 and low-temperature (<473 K) NO trapping in diesel engine emissions. ^{48–52} While the dominant active sites for methane oxidation are located on Pd nanoparticles, 7,53 isolated Pd atoms and cations are the active sites for Wacker³⁶⁻³⁸ and CO oxidation,⁵⁴ hydrodechlorination,⁵⁵ and NO trapping in passive NO_x adsorber materials.^{56,57} The redispersion of Pd nanoparticles to cations is facilitated by reactants such as NO (during NO_x reduction on TiO₂-supported three-way catalysts, ⁵⁸ H₂-selective catalytic reduction of NO on ZrO₂ supports, ⁵⁹ sequential adsorption of CO and NO on ceriazirconia supports,60 and solid-state ion-exchange in CHA zeolites⁶¹) and water (in FAU zeolites during Wacker oxidation³⁶-³⁸), and via hydrothermal treatments with steam and air in

¹Charles D. Davidson School of Chemical Engineering, Purdue University, 480 Stadium Mall Drive, West Lafayette, Indiana 47907, United States

²Department of Chemical Engineering, University of Virginia, P.O. Box 400259, Charlottesville, Virginia 22903, United States

³Department of Chemistry, Purdue University, 560 Oval Drive, West Lafayette, Indiana 47907, United States KEYWORDS Palladium, Zeolites, Nanoparticles, Redispersion, Ostwald Ripening, Kinetic Monte Carlo

aluminosilicate MFI, MWW and CHA zeolites. ⁶²⁻⁶⁴ Redispersion can be further promoted when synthesis protocols are used that promote the formation of defect or cation-exchange sites in the support that are able to capture mobile metal species emitted from nanoparticles in atom trapping processes. ^{23,24} Metal-support interactions also play a crucial role to stabilize dispersed isolated atoms, with CeO₂ and Fe₂O₃ supports exhibiting strong binding to Pt, ^{12,14,15,65,66} Rh, ¹⁵ Ru, ⁶⁷ and Cu. ^{16,68} Despite the low vapor pressure of Pd, ¹⁵ atom trapping mechanisms have been shown to stabilize isolated Pd on CeO₂, ^{11,15,55,69} TiO₂, ⁷⁰ γ-Al₂O₃, ^{7,54} and aluminosilicate zeolites. Yet, numerous questions regarding the kinetic and thermodynamic factors that influence conversion of Pd nanoparticles to single atoms and cations, and their dependence on reaction conditions, initial Pd particle size, and the metal-support interaction remain unanswered.

In this work, we examine the thermodynamic and kinetic factors and reaction mechanisms that govern the interconversion of Pd nanoparticles and cations, studying Pd supported on aluminosilicate zeolites, given that these concepts are particularly relevant for Pd-exchanged zeolites being explored in practical applications as materials for passive NO_x adsorption (PNA) ^{56,57,71} in automotive exhaust, Wacker^{36–38} and methane oxidation. 39,43,72,73 Zeolite supports are also a versatile materials platform for performing fundamental experimental studies because of the structural uniformity of their crystalline frameworks and the ability to synthesize them with precise modifications in bulk and atomic composition, which enable more faithful comparisons to the structures modeled by theoretical studies. Pd-zeolites typically contain various Pd structures 74,75 of different nuclearity (mono- and polynuclear)^{76–78} and valence (zero- to tetravalent), 79-83 but only extraframework, mononuclear cation sites charge-compensated by framework Al atoms (ion-exchanged Pd) are the purported binding sites for NO_x adsorption in the context of PNA applications⁸⁴ and the active sites for Wacker oxidation. 36-38 The structural lability of Pd allows interconversion between agglomerated domains and mononuclear ion-exchanged sites,85 which depends on the size of Pd nanoparticle domain sizes and their density on the support, 7 and causes undesirable agglomeration and deactivation under PNA and Wacker-relevant conditions. 62,86-88 Yet, such structural lability allows for the redispersion of agglomerated domains to ion-exchanged sites under high-temperature (>500 K) air⁸⁹ or NO^{61,90} regeneration. Together, these challenges and observations motivate improved fundamental understanding of the critical thermodynamic and kinetic factors that govern Pd structural interconversion in zeolites, to guide the design of these materials and regeneration protocols based on solid-state ion-exchange routes.

Here, we combine experiment and theory to understand the influence of initial Pd nanoparticle size and external gas conditions on the thermodynamic and kinetic factors influencing structural conversion between Pd nanoparticles and ion-exchanged Pd²⁺ in CHA zeolites. Pd-CHA zeolites are prepared to initially contain normally-distributed or log-normally distributed Pd particles of different mean size, located at extracrystalline zeolite surfaces. These materials are then treated to high temperatures (598–973 K) in flowing air with and without H₂O, and the number of agglomerated PdO domains and ion-exchanged Pd²⁺ sites are quantified with H₂ TPR. Density functional theory (DFT) computed thermodynamic phase diagrams are constructed for a range of Pd particle sizes under various gas environments (P_{O_2} , P_{H_2O} , temperature) to quantitatively compare with experimentally measured ion-exchanged Pd²⁺

contents on samples exposed to similar treatments to show that $\rm H_2O$ can promote the formation of PdO agglomerates from $\rm Pd^{2+}$ cations. Apparent rates of conversion of metallic Pd domains to ion-exchanged $\rm Pd^{2+}$ sites under flowing air are measured as a function of temperature (598–673 K) and $\rm H_2O$ pressure (0–2 kPa) to deduce mechanistic information and determine kinetic implications of $\rm H_2O$ and $\rm O_2$ pressures and the Pd particle size on the redispersion to ion-exchanged $\rm Pd^{2+}$ sites. Kinetic Monte Carlo (kMC) simulations are performed to rationalize the observed kinetics, and show that Pd redispersion at temperatures <900 K does not occur through a gas-phase process, but rather through a surface-mediated OR mechanism whereby mobile monomers diffuse on the zeolite support and bind at ion-trapping sites.

2. METHODS

2.1. Pd-zeolite characterization. The amounts of agglomerated PdO and mononuclear Pd2+ cations were quantified with H₂ temperature programmed reduction (TPR) procedures described elsewhere⁸⁹ using a Micromeritics AutoChem II 2920 Chemisorption Analyzer equipped with a thermal conductivity detector (TCD) to quantify H₂ consumption. In brief, the TCD response factor was generated using varied partial pressures (0.5-5.0 kPa) of H₂ in balance Ar, which quantified the amount of Ag on a Ag₂O reference material (Micromeritics) to within a factor of 1.12. After a given treatment sequence, samples (0.3-0.6 g) were exposed to flowing Ar $(0.50 \text{ cm}^3 \text{ s}^{-1}, \text{UHP}, 99.999\%,$ Indiana Oxygen) with 1-2 kPa H₂O for >0.5 h to hydrate mononuclear Pd²⁺ cations at 303 K. Samples were then cooled to 203 K (0.167 K s⁻¹) in flowing Ar (0.167 cm³ s⁻¹) using a Micromerities Cryocooler II accessory. An isopropanol slurry (cooled to 184 K with liquid N₂) was inserted between the TCD detector and the sample to trap any condensable gases. The Ar stream was replaced with 5 kPa H₂ in balance Ar (0.167 cm³ s⁻¹ ¹, certified mixture, Indiana Oxygen), and once a stable TCD signal was achieved, the sample was treated to 573 K (0.167 K s⁻¹) and held for 0.5 h. All H₂ TPR profiles and discussion of data fitting procedures are reported in Section S4, SI.

Volumetric O₂ chemisorption experiments were performed with a Micromeritics ASAP 2020 Plus Chemisorption unit. Samples (~0.2 g) were treated in flowing H₂ (UHP, 99.999%, Praxair) to 673 K or 873 K in O₂ (UHP, 99.98%, Matheson) before preparing for chemisorption. Samples were first flushed in flowing He then degassed under vacuum (< 3 µmHg) for 1 h at 373 K. Next, a leak test was performed to confirm that leak rates were below the threshold of < 600 µmHg h⁻¹ (recommended by Micromeritics). Samples were then treated in H₂ to 573 K (0.167 K s⁻¹) for 1 h, evacuated at 573 K for 1 h, then another leak test was performed at 313 K. Then, the sample was evacuated for 0.3 h at 313 K before collecting two O₂ adsorption isotherms (313 K, 2–42 kPa), with an evacuation step after the first isotherm to remove non-chemisorbed O₂. Isothermal uptakes were linearly extrapolated to zero pressure, and the difference in uptakes at zero partial pressure yielded the amount of chemisorbed O2. The dispersion was calculated assuming one O atom titrates one surface Pd atom.

2.2. Isothermal Pd Redispersion Kinetics. The as-exchanged [Pd(NH₃)₄]²⁺-CHA (2.2 wt% Pd) material was first pelleted then sieved to retain 180–250 μm diameter aggregates. Treatment sequences and H₂ TPR analysis were performed with a Micromeritics Autochem II 2920 Chemisorption Analyzer. Samples (0.03–0.05 g) were first pretreated in flowing H₂ in Ar (0.5 cm³ s⁻¹; 5 kPa H₂, certified mixture, Indiana Oxygen) to 673 K for 1 h, and cooled to ambient temperature. Samples were

then cycled through H₂ treatments, inert purge treatments, air treatments (i.e., isothermal redispersion treatments), and then the amounts of PdO and Pd²⁺ cations were quantified by H₂ TPR. As an example procedure for an isothermal redispersion measurement at 648 K in air without added H₂O, the sample was treated in flowing (0.5 cm³ s⁻¹) 5 kPa H₂ in Ar to 648 K (0.167 K s⁻¹) for 0.5 h, then the 5 kPa H₂ in Ar stream was replaced with flowing Ar (0.5 cm³ s⁻¹; UHP, 99.999%, Indiana Oxygen) to purge the system for 0.083 h. Then, the Ar stream was replaced with flowing air (0.5 cm³ s⁻¹; Air Zero, Indiana Oxygen) for a specified amount of time (0.003–1 h), and then rapidly cooled (0.67 K s⁻¹) from 648 K to ambient temperature in flowing Ar (0.5 cm³ s⁻¹) Ar using a Micromeritics Cryocooler II accessory. In cycling experiments, the air exposure times were randomly varied between 0.003-1 h to avoid any systematic errors that may have been caused by this step in the procedure.

2.3. Details of DFT, and Ab Initio Formation Free Energies Calculations. We used the Vienna ab initio simulation package (VASP, version 5.4.4)⁹¹ to perform plane-wave, periodic DFT calculations with an energy cutoff of 400 eV and projected augmented wave (PAW)⁹² pseudopotentials for core-valence interactions. We used the bulk structures reported in the Materials Project⁹³ database for metallic Pd and PdO, and the 24 T-site 1Al and 2Al Pd-exchanged SSZ13 species in the study by Mandal et al.⁹⁴ as initial guesses, and optimized them with the Perdew-Becke-Ernzerhof (PBE)95 functional and subsequently, the Heyd-Scuseria-Erzenhof (HSE06)91,95-101 hybrid exchange-correlation functional. Dispersion corrections were calculated using the Becke-Johnson damping (D3(BJ)-vdw) method. 96,97 We used the HSE06 functional with D3(BJ) dispersion corrections because it correctly captures the formation energy of PdO within 2 kJ mol⁻¹ of the experimental value (Table S5.2, SI). We used a convergence threshold of 10⁻⁸ eV and 0.01 eV/Å for the electronic energies and atomic forces, respectively. We used the Monkhorst-Pack k-point mesh detailed in the Materials Project database to sample the first Brillouin zone for bulk metallic Pd and PdO; only the Γ point was used for zeolitic structures. The optimized geometries of 6-MR 3NN Z₂H₂ and Z₂Pd have been provided in the CONTCARS attachment of the SI. Additional details about the formation energy calculations can be found in Section S5, SI.

2.4. Details of Particle Size Dependent Models. To estimate surface energies, we used the Python Materials Genomics (*Pymatgen*) package and its built-in *Slabgenerator* function $^{102-104}$ to construct symmetric slabs of up to Miller index 2 for metallic Pd and PdO from their respective optimized bulk structures. The slab thickness was set to 10 Å, and a 15 Å vacuum space was applied to eliminate interactions between the periodic images of the surfaces in the *z* direction. The k-point mesh for the slabs in the *x* and *y* directions was appropriately scaled by using the k-points per reciprocal Å for the bulk structures, with a single k-point applied in the *z* direction. We optimized and computed the energies of the unconstrained slabs using the PBE-D3(BJ)-vdw functional due to computational expense, and the same convergence criteria as that for the bulk structures. The surface energies (γ_{slab}) of the slabs were calculated as: 105

$$\gamma_{\text{slab}}(P_{0_2}, T) = \frac{E_{\text{slab}} - n_{\text{Pd}} E_{\text{bulk}} - n_{\text{O}} \mu_{\text{O}}(P_{0_2}, T)}{2A}$$
(1)

where $n_{\rm Pd}$ and $n_{\rm O}$ represent the number of Pd atoms and excess or deficit O atoms in the slab, respectively, $\mu_{\rm O}$ is the chemical potential of O, A denotes the surface area of one side of the slab, $E_{\rm slab}$ and $E_{\rm bulk}$ are the total energy of the slab and the energy of

the bulk per formula unit, respectively. The equilibrium shapes of metallic Pd and PdO nanoparticles were determined from their respective Wulff constructions which represent the minimum surface energy for a given crystal. We used the *Wulffshape* function in *Pymatgen* to generate the Wulff constructions for a range of μ_0 values, ¹⁰⁶ and evaluated the average surface energy (γ) .

Based on data fitted to calorimetric measurements of the chemical potentials of transition metals on oxide supports, Campbell et al. $^{107-109}$ expressed the free energy of supported hemispherical nanoparticles of an effective diameter d relative to bulk (ΔG) as follows:

$$\Delta G(d, P_{O_2}, T) = \left(3\gamma(P_{O_2}, T) - E_{\text{adh}}\right) \left(1 + \frac{1.5}{d}\right) \left(\frac{2\rho}{d}\right) \tag{2}$$

where ρ represents the volume normalized per mole of metal. The adhesion energy between the nanoparticle and the support $E_{\rm adh}$ is expressed according to the Young equation:

$$E_{\text{adh}} = \gamma (1 + \cos \theta) \tag{3}$$

where θ is the contact angle between the particle and support. While $\theta = 66 - 90^{\circ}$ has been reported for Pd on SiO₂, ^{110,111} it is unknown for PdO on SiO₂; therefore, we considered multiple values of $\theta = 60^{\circ}$, 90°, and 120° which are representative of varying degrees of adhesion (Figures S5.9-10, SI).

Subsequently, we evaluated the formation free energy of PdO nanoparticles ($\Delta G_{\rm PdO}^{\rm form}$) by incorporating the size-dependent free energy of PdO nanoparticles ($\Delta G_{\rm PdO}$) with respect to bulk Pd (Eq. 2) as:

$$\Delta G_{\text{PdO}}^{\text{form}} \left(d_{\text{PdO}}, P_{\text{O}_2}, T \right) = \Delta G_{\text{PdO}_{\text{bulk}}}^{\text{form}} \left(P_{\text{O}_2}, T \right) + \Delta G_{\text{PdO}} \left(d_{\text{PdO}}, P_{\text{O}_2}, T \right) - \Delta G_{\text{Pd}} \left(d_{\text{Pd}} \right)$$

$$\tag{4}$$

To relate the increment in volume associated with the formation of PdO from Pd, we used the ratio of the particle diameters of PdO and Pd ($d_{\rm PdO}/d_{\rm Pd}=1.19$) from the reported densities of bulk Pd ($\rho_{\rm Pd}=11.41~{\rm g~cm^{-3}}$) and PdO ($\rho_{\rm PdO}=7.79~{\rm g~cm^{-3}}$).

3. RESULTS AND DISCUSSION

- 3.1. Effects of initial Pd particle size and treatment conditions on the conversion of agglomerated Pd particles to exchanged Pd^{2+} ions
- 3.1.1. Synthesis of monodisperse Pd nanoparticles supported on CHA zeolites. To isolate the effects of Pd particle size on their structural interconversion to mononuclear Pd²⁺ cations that are charge-compensated by framework Al in zeolite supports (denoted "ion-exchanged Pd2+") during high-temperature air treatments, Pd particles of monodisperse size distributions were synthesized using solution-phase colloidal synthesis methods⁷ and then deposited onto the exterior of CHA zeolite crystallites (details of Pd deposition procedures in Section S1, SI). Three different colloidal Pd nanoparticle solutions were characterized with TEM to contain monodisperse particles that were nominally 2, 7, and 14 nm in diameter (Figures S2.3–S2.6, SI). These colloidal solutions were diluted in a hexane solvent and mixed with the H-form CHA zeolite powder, and then sonicated to deposit the oleylamine-capped Pd particles (denoted "as-deposited Pd-CHA"). Samples are referred to as Pd-CHA-X-ND, where X is the average particle diameter (in nm) on asdeposited samples and where the suffix ND denotes that a normal distribution of particle sizes are present initially, as determined by TEM.

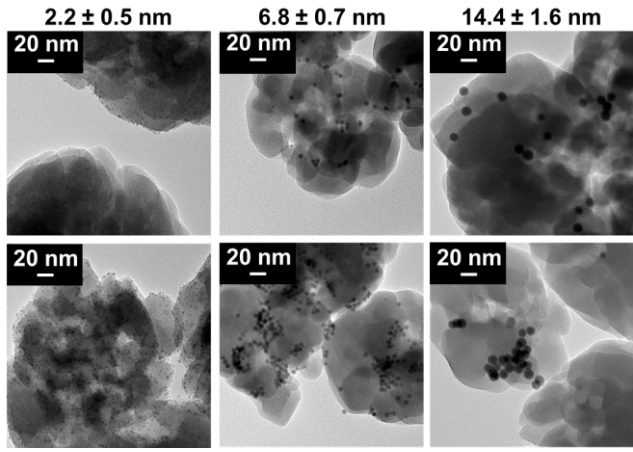


Figure 1. *Ex situ* TEM images of the as-deposited Pd-CHA-X-ND materials: Pd-CHA-2-ND (left), Pd-CHA-7-ND (middle), Pd-CHA-14-ND (right).

Figure 1 shows ex situ TEM images of the as-deposited Pd-CHA-X-ND samples, and Table 1 lists their particle size distributions and elemental analysis. Pd particle size distributions were similar on as-deposited Pd-CHA-X-ND samples as in the colloidal precursor solutions, demonstrating the deposition procedure used did not alter the monodisperse distributions of oleylamine-capped Pd nanoparticles; however, this deposition procedure did result in some non-uniformities in how Pd particles were spatially distributed at external crystallite surfaces, with some localized Pd nanoparticle aggregation observed for the Pd-CHA-7-ND and Pd-CHA-14-ND samples. To remove organic species without altering the Pd particle size distribution, as-deposited Pd-CHA-X-ND samples were first treated in air to 548 K for 4 h, before studying the effects of higher temperature air treatments. Samples treated with this protocol were analyzed in a subsequent TGA experiment and did not show desorption events for organic species (460-600 K), and TGA profiles were similar to that of the parent H-CHA support (Figures S3.1 and S3.2, SI), indicating that the majority of organic content at exterior Pd surfaces was successfully removed. TEM images of Pd-CHA-X-ND samples treated to 548 K in air showed similar Pd particle size distributions as present in their as-deposited form (Figures S2.10-S2.13, SI). Therefore, we conclude that treatment of as-deposited Pd-CHA-X-ND samples in air to 548 K successfully removed the majority of organic species while retaining the Pd particle size distribution and zeolite support intact, enabling subsequent studies of the conversion of such particles to Pd2+ cations upon treatment to higher temperatures (>548 K).

3.1.2. Effects of Pd particle size on Pd oxidation and structural interconversion. The as-deposited Pd-CHA-X-ND samples were treated to high temperatures (598–873 K) in flowing air to determine the effects of Pd particle size on the extent of oxidation with O_2 and conversion to Pd^{2+} cations. The amounts of agglomerated PdO domains and Pd^{2+} cations after high-temperature air treatments were characterized with H_2 TPR (profiles reported in Figures S4.1–S4.3, SI). Previous reports concluded that agglomerated PdO domains have a lower barrier for reduction by H_2 than hydrated Pd^{2+} ion sites; thus, H_2 consumption features can be quantified and assigned to agglomerated PdO and ion-exchanged Pd^{2+} (further discussed in Section S4, SI). 85,89,112,113

The total H₂ consumption (per total Pd) and the amount of ion-exchanged Pd²⁺ (per total Pd) after treatment in flowing air

Table 1. Characterization data on as-deposited Pd-CHA-X-ND samples. Particle size distributions are reported in Figures S2.7–S2.9, SI

Sample ^a	Nominal Pd particle size / nm	TEM characterized particle size / nm ^b	Pd wt% ^c	Pd/Al ^c
Pd-CHA-2-ND	2	2.2 ± 0.5	1.12	0.082
Pd-CHA-7-ND	7	6.8 ± 0.7	0.72	0.053
Pd-CHA-14- ND	14	14.4 ± 1.6	0.84	0.061

a Samples are denoted Pd-CHA-X-ND, where X denotes the nominal Pd particle size, and ND denotes a normal particle size distribution.

- b The average particle size plus or minus one standard deviation.
- c Pd wt% and Pd/Al molar ratio was determined by ICP.

Pd-CHA-X-ND samples are reported in Figure 2. At a given air treatment temperature, the amount of ion-exchanged Pd²⁺ formed on CHA increased as the initial Pd nanoparticle size decreased, consistent with previous reports that smaller Pd nanoparticles (at fixed Pd density) were converted to greater amounts of mononuclear Pd(OH)₂ on γ-Al₂O₃. For Pd-CHA-2-ND, the total H₂ consumed per Pd was near unity at all air treatment temperatures studied; thus, all of the 2 nm Pd nanoparticles were oxidized to Pd²⁺ during the air treatment. In contrast, Pd-CHA-7-ND and Pd-CHA-14-ND showed sub-unity H₂ consumption per Pd for low-temperature air treatments (598-673 K), suggesting that a fraction of the 7 nm or 14 nm Pd nanoparticles were not fully oxidized during the air treatment, consistent with a report by Chin et al. showing that higher O₂ pressures were needed to fully oxidize larger metallic Pd particles supported on γ-Al₂O₃ at a fixed temperature of 973 K.¹¹⁴

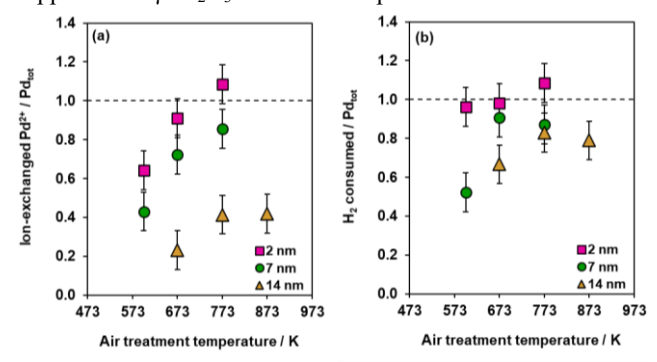


Figure 2. (a) The amount of ion-exchanged Pd²⁺ (per total Pd) after treatment in flowing air (593–873 K) for Pd-CHA-2-ND (squares), Pd-CHA-7-ND (circles), and Pd-CHA-14-ND (triangles). (b) Total H₂ consumed (per total Pd) from (a). Dashed lines represent theoretical maximum amounts. H₂ TPR profiles reported in Figures S4.1–S4.3, SI.

3.1.3. Thermodynamics of conversion of agglomerated Pd particles to exchanged Pd²⁺ ions. Estimating the maximum fraction of Pd atoms in nanoparticles that can convert to ion-exchanged Pd²⁺ based on thermodynamic considerations requires calculation of both nanoparticle and ion-exchanged zeo-lite energies. Previous studies have shown that Pd²⁺ cations charge-compensating two Al tetrahedral sites (2Al) in the six-membered ring (6-MR) are the most thermodynamically stable

ion-exchanged Pd2+ species in CHA, represented here by Z2Pd where 'Z' denotes the substitution of framework Si with Al (Figure 3).81,94,115 The lowest energy Z₂Pd structure has 2Al in a third nearest neighbor (3NN) arrangement (0 kJ mol⁻¹), followed by the 2NN configuration (+65-80 kJ mol⁻¹).81,94,115,116 One Al T-site (1Al) can be charge-compensated by Pd⁺ cations (ZPd), or by Pd²⁺ as [PdOH]⁺ (ZPdOH). The ZPd structure is +28-60 kJ mol⁻¹ higher in energy than 3NN Z₂Pd. ^{81,94} The existence of Pd⁺ after high temperature treatments in air with and without H₂O is debated in literature; 81 direct characterization of Pd⁺ has been reported only from EPR measurements of Pd/Y zeolites performed under vacuum and after H₂ treatment at 298 K.117 ZPdOH has been identified in detectable amounts only for CHA materials containing a larger number of ion-exchanged Pd²⁺ species than the number of 2Al sites in the 6-MR,⁸⁹ and is computed to be +60-79 kJ mol⁻¹ higher in energy than 3NN Z₂Pd. 81,94,116 The Pd content of the Pd-CHA-X-ND samples here (Pd/Al = 0.05-0.08) are much lower than the number of available 2Al 6-MR sites quantified by Co^{2+} titration ($Co^{2+}/Al = 0.12$). Thus, we expect Pd2+ in the 6MR 3NN configuration to be the predominant cationic species in our materials; however, for comparison, we also considered 2NN Z₂Pd, ZPd and ZPdOH in the analyses below.

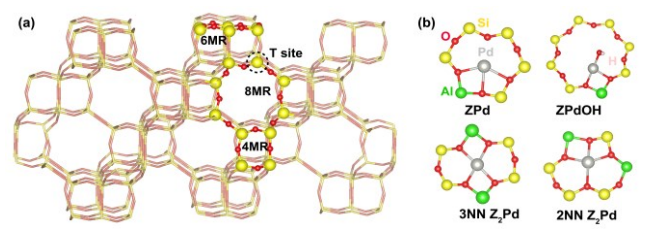


Figure 3. (a) Framework of chabazite (CHA) made up of four-, six-, and eight-membered rings (MR). (b) Pd cations exchanged at 1Al and 2Al sites.

We next computed the thermodynamics of oxidation of bulk metallic Pd (Pd_{bulk}) with O₂ to form either bulk PdO (PdO_{bulk}) or ion-exchanged Pd cations (additional details in Section S5, SI). Table 2 reports reaction energies (ΔE) and free energies (ΔG^{form}) for the formation of PdO_{bulk} from Pd_{bulk} (Eq. 5), and for the formation of 3NN Z₂Pd sites from either Pd_{bulk} (Eq. 6) or PdO_{bulk} (Eq. 7), at conditions representative of the high-temperature air treatments (598–873 K, 20 kPa O₂, impurity H₂O

Table 2. HSE06-D3(BJ)vdw-calculated 0 K formation energies (ΔE), and formation free energies of bulk PdO ($\Delta G_{\rm PdO_{\rm bulk}}^{\rm form}$), and 3NN Z2Pd ($\Delta G_{\rm Z_2Pd}^{\rm form}$) at 598 K and 873 K, 20 kPa O₂, 0.014 kPa H₂O.

Reaction	ΔE kJ (mol Po		ΔG ^{form} kJ (mol Pd) ⁻¹	
		598 K	873 K	
$ \begin{array}{c} Pd_{\text{bulk}} + \\ \frac{1}{2}O_2 \xrightarrow{\Delta G_{\text{pdO}_{\text{bulk}}}^{\text{form}}} PdO_{\text{bulk}} (5) \end{array} $	-111	-46	-16	
$Pd_{bulk} + Z_2H_2 + \frac{1}{2}O_2 \xrightarrow{\Delta G_{Z_2Pd}^{form}} Z_2Pd + H_2O (6)$	+8	-50	-74	
$PdO_{bulk} + Z_2H_2 \rightarrow Z_2Pd + H_2O $ (7)	+119	-4	-58	

estimated as 0.014 kPa H₂O) of the Pd-CHA-X-ND samples discussed in Section 3.1.2. The conversion of either Pd_{bulk} or PdO_{bulk} to 3NN Z₂Pd sites is endothermic, but thermodynamically favorable (exergonic) at temperatures >576 K (0.014 kPa H₂O, $\log_{10}(P_{O_2}/P^\circ)$ >-9.5) (Figure S5.2, SI). Reaction energies to form 2NN Z₂Pd, ZPd and ZPdOH sites are >27 kJ mol⁻¹ more endothermic than to form 3NN Z₂Pd sites (Table S5.1 and Figure S5.2, SI). These results demonstrate that conversion of bulk metallic Pd to either PdO agglomerates or to 3NN Z₂Pd sites is thermodynamically favorable over the range of high-temperature air treatments studied experimentally and suggest that the relative difference in the free energies of PdO agglomerates and Z₂Pd cations will influence Pd speciation.

To compare our thermodynamic predictions to the experimental Pd redispersion data in Figure 2, we estimated the thermodynamic limit of conversion of Pd particles to Z_2Pd (X_{Z_2Pd}) for a range of particle sizes ($d_{Pd} = 2{\text -}100 \text{ nm}$) by considering a Boltzmann distribution of the equilibrium population of PdO particles and Z_2Pd cations (Eq. 8):⁷

$$\begin{split} X_{Z_{2}Pd}(P_{O_{2}}, P_{H_{2}O}, d_{Pd}, T) &= \\ \left(\frac{N_{2Al}}{N_{Pd}}\right) \exp\left(\frac{-\Delta G_{Z_{2}Pd}^{form}(P_{O_{2}}, P_{H_{2}O}, T) - \Delta G_{PdO}^{form}(P_{O_{2}}, d_{Pd}, T)}{k_{B}T}\right) \\ \left(\frac{N_{2Al}}{N_{Pd}}\right) \exp\left(\frac{-\Delta G_{Z_{2}Pd}^{form}(P_{O_{2}}, P_{H_{2}O}, T) - \Delta G_{PdO}^{form}(P_{O_{2}}, d_{Pd}, T)}{k_{B}T}\right) + 1 \end{split}$$
(8)

where N_{2Al}/N_{Pd} is the ratio of the number of 6-MR 2Al sites as quantified by Co^{2+} titration, ¹¹⁸ and the number of Pd quantified by ICP. Analogous results for 2NN Z_2Pd , ZPd and ZPdOH are reported in Figure S5.4, SI. Particle size-dependent free energies of Pd and PdO nanoparticles were determined relative to bulk free energies using the free energy model for nanoparticles adhered to a support developed by Campbell and coworkers^{107–109} using calorimetric measurements:

$$\Delta G(d, P_{O_2}, T) = \left(3\gamma(P_{O_2}, T) - E_{\text{adh}}\right) \left(1 + \frac{1.5}{d}\right) \left(\frac{2\rho}{d}\right) \tag{9}$$

where γ is the particle surface energy (estimated from DFT), $E_{\rm adh}$ is the adhesion energy of the particle to the support (estimated from literature values and our TEM data), d is the particle diameter, and ρ is the volume normalized per mole of Pd; additional details are reported in Section 2.4. Expansion of particle volume due to the oxidation of Pd to PdO was accounted for by including a volume expansion factor of 1.19 (described in Section 2.4).

Figure 4a shows the results for the compositional parameters (N_{2Al}/N_{Pd}) and d_{Pd} corresponding to the Pd-CHA-X-ND zeolites (Table 1) and their respective air treatment conditions (Figure 2). Blue and yellow regions of Figure 4a denote complete conversion of metallic Pd particles to PdO agglomerates and to Z₂Pd sites, respectively. Figure 4a shows that complete conversion of 2 nm (squares), 7 nm (circles), and 14 nm (triangles) Pd particles to Z₂Pd is thermodynamically feasible at all the air treatment conditions in Figure 2 (598-873 K, 20 kPa O₂, 0.014 kPa H₂O), and these results are insensitive to perturbations in PdO adhesion energy (contact angle varied from 60° to 120°) and surface free energy (± 0.2 J m⁻²) within the particle sizedependent free energy model (Figures S5.5-5.6, SI). The thermodynamic predictions for 2 nm particles are consistent with the experimental results for Pd-CHA-2-ND, which contained predominantly ion-exchanged Pd²⁺ after treatment to 673 or 773 K. However, for 7 and 14 nm particles, the computed fractions of Pd particles converted to Z₂Pd sites (~1.00) are significantly higher than the amount of ion-exchanged Pd²⁺ observed

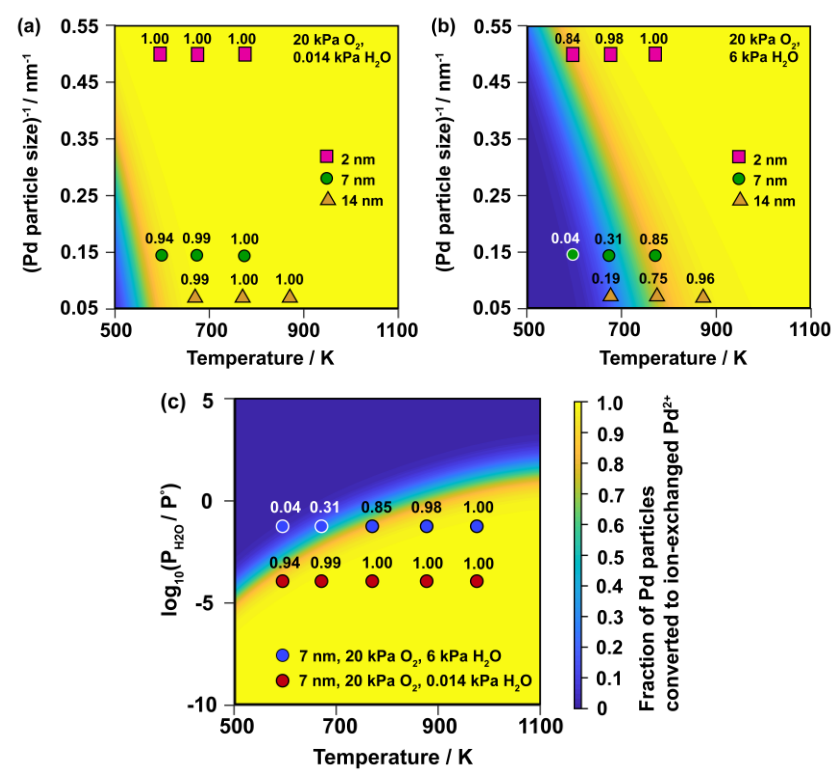


Figure 4. Pd particle size-dependent thermodynamic phase diagram for the conversion of Pd particles to Z_2Pd in CHA (Si/Al =12, Pd/Al = 0.06) under (a) 20 kPa O_2 , 0.014 kPa H_2O and (b) 20 kPa O_2 , 6 kPa H_2O , based on HSE06-D3(BJ)vdw calculated energies. The fraction of Pd particles converted to Z_2Pd for 2 nm (squares), 7 nm (circles), and 14 nm (triangles) Pd particles at the experimental air treatment conditions for Pd-CHA-X-ND samples are labeled. (c) Thermodynamic phase diagram for the conversion of 7 nm Pd particle to ion-exchanged Pd^{2+} cations on CHA (Si/Al =12, Pd/Al = 0.06) as a function of temperature and P_{H_2O} . The fraction of Pd particles converted to ion-exchanged Pd^{2+} cations at 20 kPa O_2 , 0.014 kPa P_2O (red circles), and 20 kPa O_2 , 6 kPa P_2O (blue circles) at treatment temperatures of 598-1023 K are labeled.

experimentally for Pd-CHA-7-ND and Pd-CHA-14-ND (598-773 K). Further, our model predicts complete oxidation of metallic Pd with O2 to mononuclear Pd2+ species (i.e., either agglomerated PdO or Z₂Pd) under these conditions; yet, a residual fraction of metallic Pd persists on both Pd-CHA-7-ND and Pd-CHA-14-ND following air treatments (598 K for Pd-CHA-7-ND and 598-873 K for Pd-CHA-14-ND). Air treatment of Pd-CHA-14-ND at 673 K for 1 h and 5 h formed the same amount of ion-exchanged Pd2+ and consumed the same amount of H2 per Pd (Table S4.1 and Figure S4.3, SI). These results, together with our thermodynamic modeling, suggest that complete conversion of large Pd particles (7-14 nm) to ion-exchanged Pd²⁺ is not thermodynamically limited at these conditions (598-873 K, 20 kPa O₂, 0.014 kPa H₂O), and that kinetic barriers are instead responsible for the incomplete oxidation and disintegration of large Pd particles into ion sites.

3.1.4. Effect of H₂O on the conversion of agglomerated Pd particles to exchanged Pd²⁺ ions. The addition of H₂O to the air stream has been proposed to facilitate the mobility of Pd, causing a greater fraction of agglomerated PdO domains to convert to Pd²⁺ cations. ¹¹⁹ To determine the thermodynamic influence of H₂O pressure on Pd structural interconversion, we constructed phase diagrams for air treatment conditions with higher H₂O partial pressures (6 kPa). Figure 4b shows the fraction of Pd particles converted to Z₂Pd at the different treatment temperatures studied for Pd-CHA-X-ND samples, which are labeled for comparison with Figure 4a. We considered a representative Pd particle size of 7 nm and show its conversion to Z₂Pd as a function of temperature and $P_{\rm H_2O}$ in Figure 4c at treatment conditions of 20 kPa O₂ with 0.014 kPa H₂O (red circles)

and 6 kPa $\rm H_2O$ (blue circles). Analogous phase diagrams for Pd particle sizes of 2 and 14 nm are reported in Figure S5.12, SI.

Our results predict that increasing $P_{\rm H_2O}$ thermodynamically limits the amount of Z_2Pd formed, and while the X_{Z_2Pd} values predicted vary within $\pm 20\%$ (Figures S5.9-5.11, SI) depending on the precise values used for nanoparticle adhesion and surface energy, they are consistently lower than those predicted in dry air conditions (Figure 4a). The inhibiting effect of H₂O is especially pronounced for larger Pd particles at temperatures <773 K. Our model predicts that 7 and 14 nm Pd particles almost fully convert to ion-exchanged Pd2+ during air treatments >600 K in the presence of 0.014 kPa H₂O (Figure 4a), but that the conversion of Pd particles decreases (to 0.31 and 0.19 for 7 and 14 nm, respectively) when P_{H₂O} is increased to 6 kPa (Figure 4b). Conversely, the effect of higher $P_{\rm H_2O}$ at temperatures >600 K is negligible for 2 nm Pd particles, which are predicted to fully convert to Z₂Pd during air treatments in the presence of 0.014 or 6 kPa H₂O. At conditions typically representative of practical PNA applications (2.5–6 kPa H_2O), ⁴⁸ an increase in P_{H_2O} favors formation of larger fractions of PdO agglomerates at temperatures < 800 K for $d_{Pd} = 2-14 \text{ nm}$. The H₂O promoted formation of agglomerated PdO becomes attenuated with increasing temperature due to the increase in the entropic contribution of H₂O formation relative to the enthalpy of reaction (Figure S5.13, SI). Consequently, complete conversion of Pd particles to Z₂Pd is again predicted for all the Pd-CHA-X-ND zeolites at temperatures >800 K.

Our thermodynamic predictions suggest that adding H₂O to air streams would inhibit the structural transformation of

agglomerated PdO domains to ion-exchanged Pd²⁺ cations. To experimentally test these predictions, the as-deposited Pd-CHA-7-ND sample was treated in either flowing air with 6 kPa H₂O or without H₂O at temperatures between 673–973 K, and the ion-exchanged Pd²⁺ content and H₂ consumption (per Pd) were quantified with H₂ TPR. Figure 5 and Table S4.3, SI show that fewer ion-exchanged Pd2+ sites were formed and the PdO content increased after the wet air treatment in comparison to the dry air treatment at temperatures <900 K, which is qualitatively consistent with our thermodynamic predictions (Figure 4) that increasing H₂O pressures should reduce Pd²⁺ cation content and increase the agglomerated PdO content. Similar results have been reported for atomically dispersed Pt on CeO2120 where steam exposure led to an increase in particle agglomeration. Additionally, a larger fraction of residual metallic Pd remained after wet air treatments than after dry air treatments for temperatures between 673 and 873 K, an effect that may be due to H₂O-induced hydroxylation of particle surfaces inhibiting the complete oxidation of Pd. 121 Treatment of Pd-CHA-7-ND in air at 973 K with and without H₂O resulted in the same amount of ion-exchanged Pd2+ (0.80-0.85 per total Pd) and H2 consumption (0.87–0.88 per total Pd), consistent with the absence of an H₂O pressure dependence on our thermodynamic predictions at 973 K (Figure 4). Analogous experiments on Pd-CHA-2-ND (Figures S4.4-4.5, SI) evidence no residual metallic Pd, and similar fractions of Pd2+ and PdO when either air alone or air and 6 kPa H₂O were co-fed, consistent with thermodynamic predictions that the effect of H₂O becomes attenuated for small particle sizes (Figure 4b). Together, our thermodynamic and experimental results demonstrate that co-feeding H₂O at temperatures of 673-873 K does not facilitate the transformation of PdO to ion-exchanged Pd2+, in contrast to proposals in previous studies¹¹⁹ wherein the treatment temperature itself was likely the dominant influence on the extent of agglomerated PdO converted to ion-exchanged Pd2+ cations. Instead, water promotes the formation of PdO, and this effect becomes attenuated with decreasing particle size and increasing temperature.

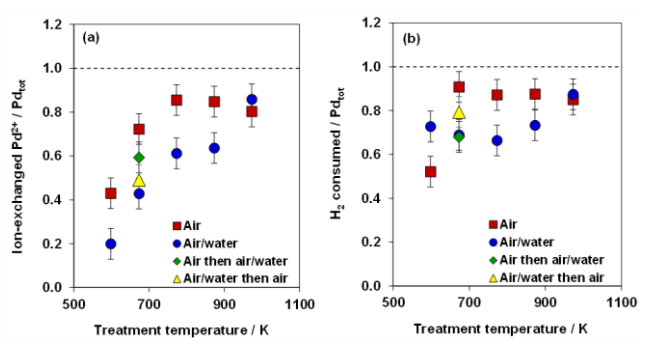


Figure 5. (a) The amount of ion-exchanged Pd^{2+} and (b) total H_2 consumed normalized per total Pd as a function of treatment temperature in flowing air (squares), 6 kPa H_2O in balance air (circles), air (1 h) then adding 6 kPa H_2O (1 h, diamond), and 6 kPa H_2O in balance air (1 h) then air (1 h, triangle) for the Pd-CHA-7-ND material. Dashed line represents theoretical maximum values. H_2 TPR profiles are reported in Figure S4.7, SI.

The decrease in cation formation when H_2O is co-fed (673–873 K) could reflect consequences of H_2O inhibiting the kinetics of Pd redispersion to Pd^{2+} cations, or changing the thermodynamic equilibrium to promote the formation of PdO agglomerates from Pd^{2+} cations, in the latter case as suggested by our thermodynamic calculations and formation of H_2O as a product

in the cation exchange reaction (Eq. 7). To determine if Pd^{2+} cations could reversibly transform to PdO agglomerates under wet conditions, the as-deposited Pd-CHA-7-ND sample was first treated in flowing dry air to 673 K and held for 1 h, and then exposed to a wet air stream (6 kPa H_2O) stream for 1 h (Figure 5, green diamond). The amount of ion-exchanged Pd^{2+} (per total Pd) decreased from 0.72 (dry air) to 0.59 (dry air followed by wet air), but did not reach the value measured on the sample exposed only to the wet air treatment (0.43). These results demonstrate that starting from a distribution of Pd^{2+} cations and PdO agglomerates the addition of H_2O to the air stream results in the loss of Pd^{2+} cations, an effect that shows that the reaction $Z_2H_2 + PdO \Leftrightarrow Z_2Pd + H_2O$ becomes reversible at 6 kPa H_2O , an effect that must be driven by thermodynamics.

To further confirm that PdO agglomerates form from Pd2+ cations under hydrous conditions, and the generality of this observation, analogous experiments were performed at 673 K and 773 K on the Pd-CHA-2-ND sample. The sample was treated in flowing dry air to 673 K and held for 1 h, and then exposed to a wet air stream (6 kPa H₂O) stream for 24 h, and the Pd speciation quantified using H₂ TPR (Figure S4.5 and Table 3). Exposure to the wet air stream decreased the fraction of ion-exchanged Pd²⁺ (per total Pd) from 0.83 (dry air) to 0.71 (dry air followed by wet air), and resulted in a concomitant increase of PdO from 0.17 (dry air) to 0.27 (dry air followed by wet air). Similar experiments performed at 773 K (Figure S4.14, Table S4.5, SI) showed an increase from 0.00 to 0.02 of the fraction of PdO after air/water exposure, consistent with the suppression of PdO formation at small particle sizes and higher temperatures predicted in Figure 4b.

Table 3. Pd speciation after 673 K and 773 K sequential air and air/water treatments on Pd-CHA-2-ND.^a

	673 K air	673 K subse- quent air/ wa- ter	773 K air	773 K subse- quent air/ water
PdO agglomerates/ Pdtot	0.17	0.27	0.00	0.02
Mononuclear Pd^{2+}/Pd_{tot}	0.83	0.71	1.08	1.00
H ₂ consumed/ Pd _{tot}	1.00	0.98	1.08	1.02

a H₂ TPR profiles reported in Figure S4.14, SI.

Introducing H₂O to the 673 K air stream after 1 h treatment of Pd-CHA-7-ND did not reversibly generate the same distribution formed after the H₂O-only treatment; moreover, a longer treatment time (18 h) in the wet air stream following an air-only treatment did not change the ion-exchanged Pd²⁺ content or H₂ consumption per total Pd (Table S4.2 and Figure S4.6, SI), demonstrating that the values reported after a 1 h treatment in Figure 5 reflect a pseudo steady-state distribution of agglomerated PdO and ion-exchanged Pd2+. Additionally, the reverse experiment was performed where the Pd-CHA-7-ND sample was first treated in wet air (6 kPa H₂O) to 673 K for 1 h, followed by removing the H₂O from the air stream and holding for 1 h. The resulting ion-exchanged Pd2+ (per total Pd) increased slightly from 0.43 (wetted air only) to 0.49, which was significantly below the result on the sample exposed only to a dry air treatment (0.72). The partially irreversible nature of Pd structural interconversion between dry and wet (6 kPa H2O) air

treatments can be rationalized from conclusions of prior work⁸⁹ that showed sample treatment history influences the spatial distribution and particle sizes of Pd domains. Here, the first dry air treatment (673 K, 1 h) of Pd-CHA-7-ND converted the 7 nm Pd particles initially present at the exterior zeolite crystallite to different PdO domain sizes and ion-exchanged Pd2+ sites distributed deeper within the interior of zeolite crystallites; thus, upon subsequent addition of H₂O to the flowing air stream, there was a different distribution of PdO particle sizes with some amount of ion-exchange Pd²⁺. Consistent with these observations, exposure of the Pd-CHA-2-ND sample to air at 1023 K, followed by air/water at 773 K did not result in formation of PdO (Figure S4.14, SI). Taken together, our results show that at low temperatures the addition of H₂O to flowing air generates a thermodynamic driving force for the reverse exchange reaction to occur (Eq. 7), forming PdO agglomerates from Pd²⁺ cations, and that the sample history and spatial distribution of Pd²⁺ sites are important factors in the extent of reversibility between Pd²⁺/PdO distributions.

3.2. Quantifying apparent rates of Pd redispersion

3.2.1. Effect of treatment temperature and H₂O on rates of Pd redispersion. To deduce mechanistic information for structural interconversion, we monitored the conversion of agglomerated, metallic Pd domains to ion-exchanged Pd²⁺ sites as a function of time under flowing air at different temperatures. To explore the effects of the functional form of the particle size distribution on redispersion rates, a suite of Pd-CHA-X-LND samples were synthesized to contain varying average particle sizes (X=2.1, and 2.9 nm), using synthesis approaches that led to a more log-normally distributed particle size distribution (denoted by 'LND' in the sample nomenclature, synthesis and characterization details in Section S1, SI) than samples prepared by colloidal Pd nanoparticle synthesis approaches.⁹⁰

Figure 6 shows the amount of ion-exchanged Pd²⁺ as a function of time and temperature for the isothermal Pd redispersion rate measurements (further discussion on rate measurements in Section S6, SI) of the Pd-CHA-2.9-LND sample. The amount of ion-exchanged Pd²⁺ formed after treatment in air for 1 h increased systematically with temperature, which agrees with thermodynamic predictions (Section 3.1.3) that higher temperatures facilitate the conversion of agglomerated PdO particles to ion-exchanged Pd2+, and is consistent with an activated process for structural interconversion. Figure 6b shows that the H₂ consumption per Pd was approximately unity for all time points after 10 s, suggesting the observed ion-exchanged Pd²⁺ formation rates were not limited by metallic Pd oxidation to PdO with O₂. This observation demonstrates the mechanistic role of O2 is only to oxidize metallic Pd; thus, the reported formation of ion-exchanged Pd2+ as a function of time reflects the rate of structural conversion of agglomerated PdO domains to ion-exchanged sites.

To determine the kinetic influence of H_2O on the apparent redispersion rate, we performed isothermal redispersion experiments on the Pd-CHA-2.9-LND sample with and without 2 kPa H_2O (Figure 7). Consistent with previous thermodynamic arguments, adding 2 kPa H_2O to the inlet air stream decreased the amount of ion-exchanged Pd^{2+} cations after treatment for 1 h (Figure S6.1, SI); however, when the amount of exchange was normalized to the pseudo steady-state value after 1 h (i.e., normalizing rates to the reversible fraction of Pd that can interconvert), the apparent rates of redispersion with and without H_2O

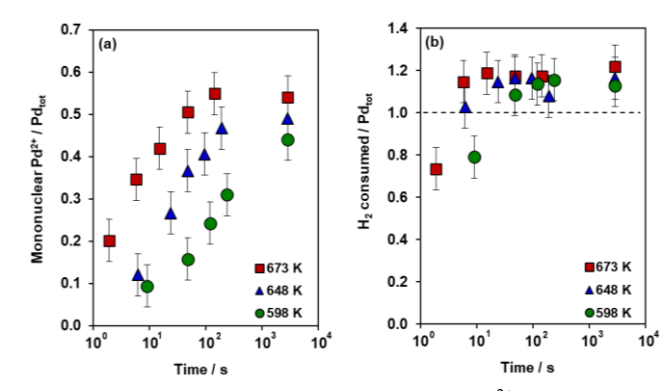


Figure 6. (a) The amount of ion-exchanged Pd²⁺ normalized per total Pd as a function of time during isothermal switching experiments for three different treatment temperatures (square: 673 K, triangle: 648 K, circle: 598 K) using the Pd-CHA-2.9-LND sample, (b) The total H₂ consumed normalized per total Pd from (a). Dashed line represents theoretical maximum amount. H₂ TPR profiles are in Figures S4.9–S4.11, SI.

were similar within error. Additionally, the H₂ consumption per total Pd was approximately unity for all time points measured, again demonstrating the rate of Pd redispersion was not limited by Pd oxidation. Therefore, co-feeding H₂O did not have a significant kinetic effect on the redispersion of PdO particles to ion-exchanged Pd²⁺ and, for this material and conditions of these measurements, H₂O apparently only influences the thermodynamics of the redispersion process.

Time-dependent redispersion measurements of the Pd-CHA-2.1-LND sample (Figure 7) showed faster apparent rates of redispersion to ion-exchanged Pd²⁺. Notably, the shortest time point of 10 s resulted in almost complete conversion (0.9) of the Pd species that reversibly convert between agglomerated domains and ion-exchanged Pd²⁺. Additionally, all the redispersion rates measured for Pd-CHA-2.1-LND showed H₂ consumptions per Pd near unity. These data suggest smaller Pd nanoparticles disintegrate at a faster rate for structural interconversion to ion-exchanged Pd²⁺.

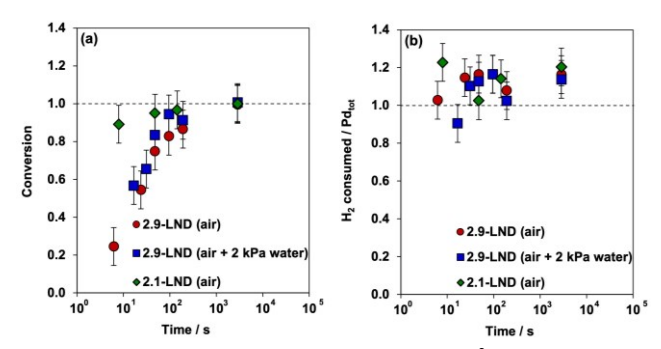
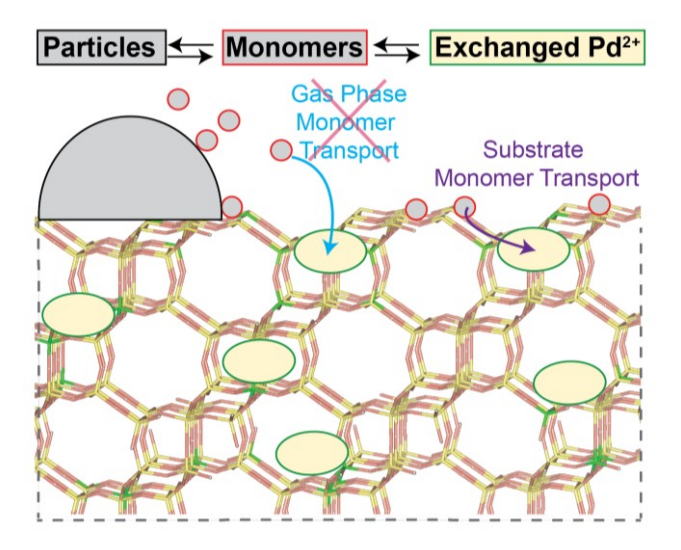


Figure 7. (a) The amount of ion-exchanged Pd^{2+} (normalized per ion-exchanged Pd^{2+} content after treatment for 1 h, and denoted as conversion) as a function of time during isothermal switching experiments performed at 648 K for Pd-CHA-2.9-LND sample in air (circles), 2 kPa H₂O in balance air (squares), and Pd-CHA-2.1-LND in air (diamonds). H₂ TPR profiles are in Figures S4.10, S4.12, and S4.13, SI. (b) H₂ consumed normalized to total Pd of materials in (a).

3.2.2. Kinetic models for Pd redispersion. Experimental data and atomistic simulation results for supported metal particles suggest that Ostwald ripening (OR) is the predominant mechanism for the disappearance of small nanoparticles and

sintering compared to particle migration and coalescence.^{22,122} The OR process is associated with the rapid disappearance of particles smaller than a critical radius, generating a pool of monomers that transport between particles through either gas phase or surface diffusion processes, resulting in the formation of larger particles. In contrast to conventional OR mechanisms, in the presence of framework Al ion-exchange sites in the zeolite support, we hypothesize that monomers ejected from the surface of PdO particles form either larger PdO agglomerates or ion-exchanged Pd²⁺ via an atom trapping mechanism (Scheme 1). Figures 6 and 7 demonstrate that oxidation of metallic Pd to PdO is rapid relative to the rate of redispersion to Pd²⁺ cations, therefore we consider PdO to be the initial state of the particles in the redispersion mechanism. Plausible monomer-facilitated mechanisms proposed for the conversion of PdO nanoparticles to ion-exchanged Pd2+ involve the detachment of neutral, mobile species, such as Pd₁O₁ and Pd₁(OH)₂ from PdO agglomerates, and their successive reactions with the zeolitic Brønsted acid sites. 7,89,123 There are established kinetic models for ORbased particle sintering for supported metal catalysts, 27,124,125 however, kinetic models have not been reported that incorporate monomer migration and subsequent atom trapping of monomers on surface/lattice defect or cation exchange sites.

Scheme 1. Proposed scheme for Pd ion exchange via monomers generated from Ostwald ripening.



Ripening of nanoparticles occurs by diffusion of monomers through the gas phase or on a substrate. 27,126-132 Wynblatt and Gjostein proposed that monomer transport via the gas phase takes place for metals with volatile metal oxides such as Pt. 124 Simulation results reported by Plessow et al. for dispersed Pt particles on silica using a modified Wynblatt-Gjostein gasphase sintering model show agreement with the experimental data in the high-temperature regime (>1023 K) where higher oxygen pressures accelerated sintering via formation of volatile Pt₁O₂(g). 133 Recently, Goodman et al. performed similar gasphase sintering simulations for Pd/SiO₂ to demonstrate that emission of Pd atoms in the vapor phase becomes substantially higher (5 atoms s⁻¹ from a 8.8 nm Pd particle) with an increase in Pd vapor pressure at temperatures >1173 K. 134 Although the air treatment temperatures reported here (598-1023 K) are lower than those where gas-phase sintering has been shown to become appreciable, we explored the possibility of both gasphase and substrate-mediated Pd redispersion.

To determine the feasibility of a gas phase OR process, we next computed the rate of formation of the most stable gasphase Pd monomer, which was found to be $Pd(OH)_2(g)$ (details in Section S8.1.1, SI), consistent with prior reports. We estimated the pressure (P_k) of ejected $Pd(OH)_2(g)$ monomers in equilibrium with a PdO nanoparticle comprised of k atoms as:

$$PdO_{\text{bulk}} + H_2O \xrightarrow{\Delta G_{Pd(OH)_2(g)}^{\text{form}}} Pd(OH)_2(g)$$
 (10)

$$P_k = P_{\text{H}_2\text{O}} \exp\left(\frac{-\Delta G_{\text{Pd(OH)}_2(g)}^{\text{form}} + \frac{A_k \gamma}{k}}{k_B T}\right)$$
(11)

where γ is the average surface energy of the PdO surface from which monomers detach, A_k is the surface area of the particle, and $\Delta G_{\rm Pd(OH)_2(g)}^{\rm form}$ denotes the formation free energy of Pd(OH)₂(g) relative to bulk PdO. For a system with a distribution of particle sizes, the background pressure $(P_{\rm b})$ of Pd(OH)₂(g) is given by: 128

$$P_{\rm b} = \frac{\sum_k A_k n_k P_k}{\sum_k A_k n_k} \tag{12}$$

where n_k is the surface density of the nanoparticle, and P_k is the equilibrium pressure of monomers calculated using Eq. 11. Subsequently, the influx of Pd(OH)₂(g) monomers J_k (monomers nm⁻² s⁻¹) received by a PdO nanoparticle comprised of k atoms can be estimated using kinetic theory of gases:

$$J_k = \frac{(P_b - P_k)}{\sqrt{2\pi m_{Pd(OH)_2(g)} k_B T}}$$
 (13)

where $m_{Pd(OH)_2(g)}$ is the molecular mass of Pd(OH)₂(g). A lower background monomer pressure would correspondingly result in a lower monomer flux. For example, at 6 kPa H₂O, 20 kPa O₂, and 873 K, the particle size distribution for the Pd-CHA-7-ND sample (Figure S2.8, SI) generates a background monomer pressure of only 3.2×10^{-16} kPa, and 3.6×10^{-7} Pd(OH)₂ (g) monomers per second colliding with the surface of a 7 nm particle in the distribution. In comparison, a similar Pt particle size distribution has a collision frequency of 25 PtO₂ (g) monomers s⁻¹ because of its substantially higher background monomer pressure (2.8×10^{-8} kPa). We also considered other plausible scenarios (e.g. PdO(g)) for gas phase monomer formation (Table S8.2, SI), but all such routes have fluxes that are even lower than the formation of Pd(OH)₂(g) from PdO agglomerates. The maximum rates of ion-exchange (Section S8.1.3, SI) for the Pd-CHA-7-ND and Pd-CHA-2.9-LND samples (Figure 7) are 10^{-15} s⁻¹ (673 K, $d_{\rm avg} = 7$ nm), and 10^{-13} s⁻¹ (648 K, $d_{\rm avg} = 2.9$ nm), respectively. The observed rate of ionexchange for Pd-CHA-2.9-LND (~10⁻⁴ s⁻¹) and the time scale reported in our experiments (Figure 2) for complete ion-exchange of Pd-CHA-7-ND (~1 h) are orders of magnitude faster than the computed gas phase rates.

The available data show that Pd redispersion does not occur through the gas phase at temperatures <900 K. First, the observed redispersion rates at the conditions of our experiments are at least ~9 orders of magnitude faster than what would be expected for a gas phase process. Challa et al. 129 invoked similar calculations for emission of Ni monomers to show that monomers transport on the support during the disappearance of small Ni nanoparticles supported on MgAl₂O₃. Second, since Pd(OH)₂(g) monomer flux is directly proportional to $P_{\rm H_2O}$ in a gas phase process (Eq.s 10 and 11) changes in $P_{\rm H_2O}$ should reflect changes on the rates of formation of ion-exchanged Pd²⁺.

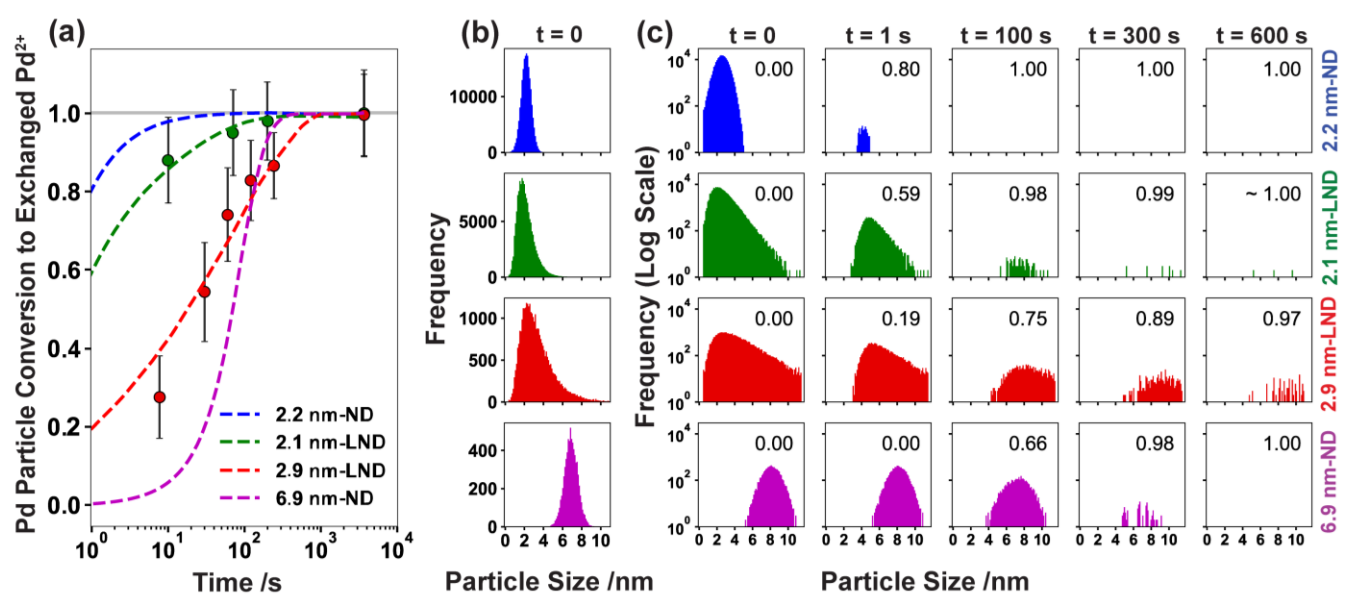


Figure 8. (a) The kMC predicted redispersion kinetics at T=648 K. Model parameters were estimated by fitting the 2.9 nm averaged lognormally distributed (LND) sample (red traces) to experimentally measured conversion (red circles). The error bars denote one standard deviation of experimental measurements. (b) Initial simulated Pd particle size distributions. (c) The evolution of PdO particle size distributions as a function of time, the number on the top right in each histogram shows the conversion of Pd atoms in PdO particles to exchanged Pd²⁺. Simulation results for t<1 s are shown in Figure S8.4, SI.

For example, comparison of experimental and simulation results for isothermal Pt sintering (873 K) showed faster rates of sintering with increases in P_{0_2} . ¹³³ However, as evidenced by the results of the isothermal redispersion air treatment with and without 2 kPa H₂O (Figure 7), there was no change in the apparent rates of redispersion, again suggesting that diffusion of monomers on the zeolite substrate is the dominant process. Finally, if the OR process occurred via gaseous monomers, it would be expected that all oxidized Pd would disintegrate and form cations, but this is not the case as demonstrated in Figure 2. Taken together, these results imply that interconversion of Pd particles to ion-exchanged Pd occurs through diffusion of monomer species on the zeolite substrate at temperatures <900 K.

To elucidate the particle size dependent nature of the redispersion of PdO agglomerates and ion exchange process, we next incorporated an atom trapping surface reaction assumed to be first order in both Z_2H_2 exchange sites and mean-field substrate monomer concentration:

$$\frac{d\mathbf{Z}_2\mathbf{H}_2}{dt} = -k_{rxn}[\mathbf{Z}_2\mathbf{H}_2][\text{monomer}] \tag{14}$$

into the system of differential equations that correspond to the mass balance of a substrate-mediated OR kinetic model $^{127-129}$ that accounts for activated monomer formation, activated diffusion of monomers on a substrate, and exchange of monomers between particles comprised of k Pd atoms:

$$\frac{dC_k}{dt} = -K_{os}C_{inf} \left[\exp\left(\frac{\Delta G_{k*}}{k_B T}\right) - \exp\left(\frac{\Delta G_k}{k_B T}\right) \right] C_k d_k +$$
generation) (15)

where, C_k is the particle number density (particles nm⁻²), ΔG_k is the nanoparticle free energy with respect to bulk PdO (computed using the relation developed by Campbell et al. in Eq. 9), K_{os} is the lumped pre-exponential factor for OR, C_{inf} is the farfield concentration of monomers in equilibrium with an infinite size particle at an infinite distance from the particle-support interface, and d_k is the effective particle diameter (Table S8.1,

SI). Full details of the OR kinetic model are reported in Section S8.2, SI. Depending on the number of Pd atoms that correspond to the critical particle radius (k_* , determined at each time step as described in Section S8.2, SI), a particle will either grow ($k > k_*$) by consuming monomers or shrink ($k < k_*$) by detaching monomers. The generation term represents formation of a new particle with k Pd atoms:

(generation) =
$$\begin{cases} -\frac{dc_{k-1}}{dt} & \text{if } k > k_* \\ 0 & \text{if } k = k_* \\ +\frac{dc_{k+1}}{dt} & \text{if } k < k_* \end{cases}$$
 (16)

Eq. 15 shows that the driving force for the OR process, $\left[\exp\left(\frac{\Delta G_{k*}}{k_{\rm B}T}\right) - \exp\left(\frac{\Delta G_k}{k_{\rm B}T}\right)\right]$, originates from the free energy difference between nanoparticles of different sizes. The resulting monomer mass balance is:

$$\frac{d \text{ [monomer]}}{dt} = \frac{d [Z_2 H_2]}{dt} + \sum_0^{N < k*} \frac{dC_k}{dt} - \sum_0^{N > k*} \frac{dC_k}{dt}$$
(17)

and describes monomer consumption due to atom trapping at Z_2H_2 sites, generation of monomers from smaller particles, and consumption of monomers by larger particles.

The four model parameters are the rate constant for cation exchange from monomers $(k_{rxn}, \text{nm}^2 \text{s}^1)$, the OR rate constant associated with activated diffusion of monomers $(K_{os}, \text{nm}^2 \text{s}^1)$, the far-field concentration of monomers $(C_{inf}, \text{nm}^2 \text{ related to})$ the monomer formation energy), and the surface energy of the nanoparticles $(\gamma, \text{J m}^2 \text{ implicit in } \Delta G_k)$. Typical reported values for these parameters are shown in Table S8.5, SI. We randomly generated initial Pd particle size distributions that are consistent with the log-normal distribution (LND) means and standard deviations of the experimentally observed particle size distributions for the Pd-zeolite samples in Figure 7 (Table S2.1, SI). We started by assuming these particles oxidize rapidly and their initial state is PdO, as evidenced by Figures 6b and 7b, and then

used kinetic Monte Carlo (kMC) to solve the resulting system of differential equations (Section S8.2, SI) for the particle size distribution, monomer concentration, and the fraction of ion exchange as a function of time. The randomly generated particle size distributions, and kMC itself, give stochastic results; therefore, the results from 350 independent kMC simulations were averaged to generate predictions for the fractional extent of ion exchange. Figure S8.3, SI shows that by 250 kMC simulations results are converged. We regressed the four model parameters using only the measured conversion of Pd-CHA-2.9-LND (Figure 7); regressed OR parameter values fall into the ranges of those previously reported (Table S8.5, SI) and the regressed surface energy is within 0.1 J m⁻² of our DFT-computed value.

Figure 8 reports kMC results starting from a log-normal distribution (LND) of nanoparticles, consistent with the samples prepared via incipient wetness impregnation (Pd-CHA-2.1-LND (red traces), Pd-CHA-2.9-LND (green traces)), or a normal distribution (ND), consistent with the samples prepared from monodisperse Pd particles via colloidal synthesis (Pd-CHA-2-ND (blue traces, 2.2 nm, particle size distribution in Figure S2.7, SI), Pd-CHA-7-ND (purple traces, 6.9 nm, particle size distribution in Figure S2.8, SI)). The model predicts that larger particles (2.9 nm) have slower rates of ion-exchange compared to the smaller particles (2.1 nm) and captures the differences in rate between the two particle size distributions that are observed experimentally (Figure 7). We emphasize that the regressed model parameters are not particle size-dependent, and the effect of particle size on kinetics is described solely by the physics of OR and atom trapping in the model. Smaller particles result in a higher substrate monomer concentration, which drives the exchange reaction, and has a strong dependence on particle size. As released monomers are consumed by the faster trapping reaction the particles continue to lose monomers onto the substrate, and the exchangeable fraction of Pd for all distributions is completely exhausted within 1000 s. Figure 8b shows that the narrower particle size distributions for the ND samples (Pd-CHA-2-ND) result in faster rates of ion exchange compared to the LND samples with similar average particle size (Pd-CHA-2.1-LND and Pd-CHA-2.9-LND), because the largest particles located in the trailing tail of the LND particle size distribution are the slowest to disintegrate. The Pd-CHA-7-ND sample is predicted to reach complete conversion of exchangeable Pd by 400 s, which is consistent with experimental observations that full ion-exchange is reached within 1 h. The model predicts the Pd-CHA-7-ND sample will reach complete conversion more rapidly than the Pd-CHA-2.9-LND, highlighting the effect of size distribution. The Pd-CHA-7-ND sample has a longer induction period than Pd-CHA-2.9-LND (Figure S8.4, SI), however, once redispersion starts, the majority of particles in a tighter distribution will quickly release monomers. Although the unexchangeable fraction of Pd reported in Figure 2 is not accounted for in our kinetic model, the substrate-mediated OR model accurately describes the kinetics of the exchangeable Pd fraction, suggesting that the experimentally observed incomplete ion-exchange likely reflects the non-mean-field nature of diffusion through a porous three-dimensional substrate and the spatial arrangement of particles at external zeolite crystallite surfaces. The K_{os} and k_{rxn} parameters depend on interparticle distances, and distances between particles and exchange sites, respectively, and their regressed values represent a weighted average over different local environments of particles in the samples. These parameters may vary with changes in the spatial distribution of particles^{7,135} and exchange sites, and do not

account for pore blocking, which may result in incomplete ion-exchange. 136,137 Further, the molecular structure(s) of the monomer intermediates formed on the zeolite substrate are unknown; their energetics in our model are described by the regressed k_{rxn} , K_{os} , and C_{inf} parameters. Nevertheless, our kinetic model captures the observed kinetic dependence of redispersion on particle size and demonstrates that integration of atom trapping kinetics with an OR kinetic model is consistent with the available experimental data.

4. CONCLUSIONS

We combined precise catalyst synthesis techniques, quantitative site characterization methods, and computational thermodynamic and kinetic models to examine the relative importance of the thermodynamic and kinetic factors governing the interconversion of Pd nanoparticles and ion-exchanged Pd²⁺ cation sites in CHA zeolites under high temperature (593-973 K) air treatments with and without H₂O. To facilitate quantitative measurements of Pd particle redispersion rates and their dependence on the Pd initial particle size and particle size distribution, we prepared a series of Pd-CHA materials using two different synthetic approaches; deposition of colloidal Pd nanoparticle suspensions to form monodisperse, normally distributed Pd particles of different sizes (2-14 nm), and incipient wetness impregnation yielding log-normally distributed particles of varying average sizes (2.1 and 2.9 nm). Smaller Pd nanoparticles (2 nm) readily converted to ion-exchanged Pd²⁺ species in air. The conversion of larger metallic Pd nanoparticles (7, 14 nm) to PdO domains and ion-exchanged Pd2+ was observed to be lower than the thermodynamic distributions predicted by DFT, indicating that larger metallic particles have kinetic barriers for oxidation with O2 to PdO and for the subsequent disintegration of PdO to ion-exchanged Pd2+ sites. Additionally, increasing the H₂O partial pressure shifts the thermodynamic distribution away from Pd2+ sites and toward agglomerated PdO domains, suggesting that H₂O present in exhaust streams facilitates Pd deactivation to PdO agglomerated phases. Our results suggest that the widely observed agglomeration and deactivation of Pd cation-exchanged zeolites in low temperature hydrous environments (e.g. Wacker oxidation, automotive exhaust, and PNAs) reflect thermodynamic factors that may be deleterious to the long-term storage and stability of atomicallydispersed Pd-zeolite materials.

To deduce mechanistic information of the Pd redispersion process, quantitative measurements of Pd nanoparticle conversion to ion-exchanged Pd2+ sites in air with and without H2O were performed isothermally (598-673 K) with varying treatment time (0.003–1.0 h). The oxidation of metallic Pd with O_2 is complete after 0.003 h of treatment time, and thus kinetically irrelevant for apparent rates of PdO conversion to ion-exchanged Pd²⁺ sites. Additionally, a predominantly PdO-containing CHA material treated in either inert (He) or air to 648 K resulted in similar extents of PdO conversion to ion-exchanged Pd2+, further reinforcing that the dominant mechanistic role of O₂ is to oxidize agglomerated metallic Pd to PdO. In the presence of H₂O, the extent of interconversion from Pd²⁺ to PdO is lower when following higher temperature pretreatments, suggesting that Pd²⁺ ions located deeper in the zeolite crystallite are kinetically inaccessible at these conditions.⁸⁹ Under these conditions, quantum chemical calculations predict Pd(OH)₂(g) is the most thermodynamically favorable gaseous Pd species, suggesting that adding H₂O to the air stream may facilitate hydroxylation of the PdO surface to increase the rate of forming Pd(OH)₂(g) intermediates. However, computed rates of gas-

phase redispersion kinetics are orders of magnitude slower than experimentally observed rates, and experiments performed with H₂O (2 kPa) added to the air stream (648 K) show that H₂O pressure (0-2 kPa) did not influence Pd redispersion rates normalized by the fraction of Pd that reversibly interconverts between particles and cation sites. These observations show that H₂O strongly influences the thermodynamics, but not the kinetics, of Pd structural interconversion at 648 K. Smaller Pd nanoparticles result in faster disintegration rates and a greater thermodynamic driving force to form ion-exchanged Pd²⁺. Our kMC simulations of a surface-diffusion mediated OR process, with exchange of mobile Pd species at ion-trapping sites in the zeolite support (formed by Al substitution), are consistent with the particle size dependent kinetics observed experimentally and capture the observed trends with respect to particle size and distribution. Monodisperse particles exhibited faster rates of redispersion compared to log-normally distributed Pd particles because the largest particles in the tail of the distribution require the longest time to disintegrate to monomers.

We conclude that gas phase conditions, initial Pd nanoparticle sizes, and particle size distributions (ND vs. LND), influence the critical thermodynamic and kinetic factors that govern Pd redispersion to ion-exchanged Pd²⁺ sites, which are the desired precursor Pd structures for PNA, Wacker oxidation, and other applications. More broadly, we show that low-temperature (<900 K) Pd redispersion does not occur through gas-phase intermediates, but rather a surface-mediated OR process in the presence of atom trapping sites, as recently suggested by Datye and coworkers for noble metals on ceria supports.² Our results suggest that at low temperatures (<900 K), similar processes may govern the redispersion of Pd nanoparticles on other oxide supports; thus, the non-mean field nature of diffusion on the support and the spatial distribution of particles and atom or ion trapping sites are important factors to consider in strategies to enhance or suppress the rate of redispersion of Pd and PdO particles into site-isolated cations.

ASSOCIATED CONTENT

Supporting Information

The Supporting Information is available free of charge on the ACS Publications website.

Supporting_Information.pdf Supplementary details referred to in the main text (PDF)

CONTCARS.zip

Optimized geometries of 6-MR 3NN Z₂H₂ and Z₂Pd (ZIP)

AUTHOR INFORMATION

Corresponding Author

*cp9wx@virginia.edu, *rgounder@purdue.edu

Author Contributions

†T. M. L. and K. M. contributed equally.

ACKNOWLEDGMENT

The authors acknowledge the financial support from the Department of Energy, Energy Efficiency and Renewable Energy (DE-EE0008213) for the experimental work at Purdue (R.G., T.M.L.,

H.L., B.K.B.), and from the NSF under Cooperative Agreement EEC-1647722 and the Engineering Research Center for the Innovative and Strategic Transformation of Alkane Resources (CISTAR) for the Pd nanoparticle synthesis and characterization work at Purdue (C.L., V.Y). The authors also acknowledge the UVA Engineering Research and Innovation Award (K.M., C.P.) and the Double Hoo Research Grant (K.M.) for financial support throughout the development of this project, and the National Science Foundation Faculty Early Career Development Program under award number 2144174-CBET (C.P.). The authors acknowledge Research Computing at the University of Virginia for the computational resources and technical support, and Prof. Robert J. Davis and William S. Epling for helpful technical discussions. Additionally, the Purdue co-authors thank Dr. Xinyi Wei (BASF Corporation) for providing the CHA material and all other members of the collaborative research team from the University of Kentucky, University of California Berkeley, Ford Motor Company, Oak Ridge National Laboratory, and BASF for helpful technical discussions.

REFERENCES

- (1) Liu, L.; Corma, A. Evolution of Isolated Atoms and Clusters in Catalysis. *Trends Chem.* **2020**, *2* (4), 383–400.
- (2) Datye, A. K.; Guo, H. Single Atom Catalysis Poised to Transition from an Academic Curiosity to an Industrially Relevant Technology. *Nat. Commun.* 2021 121 2021, 12 (1), 1–3.
- (3) Liu, L.; Corma, A. Confining Isolated Atoms and Clusters in Crystalline Porous Materials for Catalysis. *Nat. Rev. Mater.* 2020 63 2020, 6 (3), 244–263.
- (4) Li, Z.; Ji, S.; Liu, Y.; Cao, X.; Tian, S.; Chen, Y.; Niu, Z.; Li, Y. Well-Defined Materials for Heterogeneous Catalysis: From Nanoparticles to Isolated Single-Atom Sites. *Chem. Rev.* **2020**, *120* (2), 623–682.
- (5) Liu, L.; Corma, A. Metal Catalysts for Heterogeneous Catalysis: From Single Atoms to Nanoclusters and Nanoparticles. *Chem. Rev.* 2018, 118 (10), 4981–5079.
- (6) Wang, A.; Li, J.; Zhang, T. Heterogeneous Single-Atom Catalysis. Nat. Rev. Chem. 2018 26 2018, 2 (6), 65–81.
- Goodman, E. D.; Johnston-Peck, A. C.; Dietze, E. M.; Wrasman, C. J.; Hoffman, A. S.; Abild-Pedersen, F.; Bare, S. R.; Plessow, P. N.; Cargnello, M. Catalyst Deactivation via Decomposition into Single Atoms and the Role of Metal Loading. *Nat. Catal.* 2019, 2 (9), 748–755.
- (8) Nie, L.; Mei, D.; Xiong, H.; Peng, B.; Ren, Z.; Hernandez, X. I. P.; DeLaRiva, A.; Wang, M.; Engelhard, M. H.; Kovarik, L.; Datye, A. K.; Wang, Y. Activation of Surface Lattice Oxygen in Single-Atom Pt/CeO2 for Low-Temperature CO Oxidation. Science (80-.). 2017, 358 (6369), 1419–1423.
- (9) Fernández, E.; Liu, L.; Boronat, M.; Arenal, R.; Concepcion, P.; Corma, A. Low-Temperature Catalytic NO Reduction with CO by Subnanometric Pt Clusters. ACS Catal. 2019, 9 (12), 11530– 11541
- (10) Liu, L.; Zakharov, D. N.; Arenal, R.; Concepcion, P.; Stach, E. A.; Corma, A. Evolution and Stabilization of Subnanometric Metal Species in Confined Space by in Situ TEM. *Nat. Commun.* 2018 91 2018, 9 (1), 1–10.
- (11) Yuan, K.; Guo, Y.; Huang, L.; Zhou, L.; Yin, H.-J.; Liu, H.; Yan, C.-H.; Zhang, Y.-W. Tunable Electronic Metal–Support Interactions on Ceria-Supported Noble-Metal Nanocatalysts in Controlling the Low-Temperature CO Oxidation Activity. *Inorg. Chem.* **2020**, *60* (7), 4207–4217.
- (12) Jones, J.; Xiong, H.; DeLaRiva, A. T.; Peterson, E. J.; Pham, H.; Challa, S. R.; Qi, G.; Oh, S.; Wiebenga, M. H.; Hernández, X. I. P.; Wang, Y.; Datye, A. K. Thermally Stable Single-Atom Platinum-on-Ceria Catalysts via Atom Trapping. Science (80-.). 2016, 353 (6295), 150–154.
- (13) Jeong, H.; Bae, J.; Han, J. W.; Lee, H. Promoting Effects of Hydrothermal Treatment on the Activity and Durability of Pd/CeO2 Catalysts for CO Oxidation. ACS Catal. 2017, 7 (10), 7097–7105.
- (14) Xiong, H.; Lin, S.; Goetze, J.; Pletcher, P.; Guo, H.; Kovarik, L.; Artyushkova, K.; Weckhuysen, B. M.; Datye, A. K. Thermally

- Stable and Regenerable Platinum—Tin Clusters for Propane Dehydrogenation Prepared by Atom Trapping on Ceria. *Angew. Chemie Int. Ed.* **2017**, *56* (31), 8986–8991.
- (15) Alcala, R.; DeLaRiva, A.; Peterson, E. J.; Benavidez, A.; Garcia-Vargas, C. E.; Jiang, D.; Pereira-Hernández, X. I.; Brongersma, H. H.; Veen, R. ter; Staněk, J. et alAtomically Dispersed Dopants for Stabilizing Ceria Surface Area. Appl. Catal. B Environ. 2021, 284, 119722.
- (16) Yu, W.-Z.; Wang, W.-W.; Li, S.-Q.; Fu, X.-P.; Wang, X.; Wu, K.; Si, R.; Ma, C.; Jia, C.-J.; Yan, C.-H. Construction of Active Site in a Sintered Copper–Ceria Nanorod Catalyst. J. Am. Chem. Soc. 2019, 141 (44), 17548–17557.
- (17) Carter, J. H.; Liu, X.; He, Q.; Althahban, S.; Nowicka, E.; Freakley, S. J.; Niu, L.; Morgan, D. J.; Li, Y.; Niemantsverdriet, J. W. (Hans) et alActivation and Deactivation of Gold/Ceria–Zirconia in the Low-Temperature Water–Gas Shift Reaction. Angew. Chemie Int. Ed. 2017, 56 (50), 16037–16041.
- (18) Deng, W.; Frenkel, A. I.; Si, R.; Flytzani-Stephanopoulos, M. Reaction-Relevant Gold Structures in the Low Temperature Water-Gas Shift Reaction on Au-CeO2. J. Phys. Chem. C 2008, 112 (33), 12834–12840.
- (19) Malta, G.; Kondrat, S. A.; Freakley, S. J.; Davies, C. J.; Lu, L.; Dawson, S.; Thetford, A.; Gibson, E. K.; Morgan, D. J.; Jones, W. et al Identification of Single-Site Gold Catalysis in Acetylene Hydrochlorination. *Science* 2017, 355 (6332).
- (20) Malta, G.; Kondrat, S. A.; Freakley, S. J.; Davies, C. J.; Dawson, S.; Liu, X.; Lu, L.; Dymkowski, K.; Fernandez-Alonso, F.; Mukhopadhyay, S.; Gibson, E. K.; Wells, P. P.; Parker, S. F.; Kiely, C. J.; Hutchings, G. J. Deactivation of a Single-Site Gold-on-Carbon Acetylene Hydrochlorination Catalyst: An X-Ray Absorption and Inelastic Neutron Scattering Study. ACS Catal. 2018, 8 (9), 8493–8505.
- (21) Shan, J.; Li, M.; Allard, L. F.; Lee, S.; Flytzani-Stephanopoulos, M. Mild Oxidation of Methane to Methanol or Acetic Acid on Supported Isolated Rhodium Catalysts. *Nat. 2017 5517682* 2017, 551 (7682), 605–608.
- (22) Hansen, T. W.; Delariva, A. T.; Challa, S. R.; Datye, A. K. Sintering of Catalytic Nanoparticles: Particle Migration or Ostwald Ripening? Acc. Chem. Res. 2013, 46 (8), 1720–1730.
- (23) Xiong, H.; Datye, A. K.; Wang, Y. Thermally Stable Single-Atom Heterogeneous Catalysts. *Adv. Mater.* **2021**, 2004319.
- (24) Datye, A. K. Dispersing Nanoparticles into Single Atoms. *Nat. Nanotechnol.* 2019 149 2019, 14 (9), 817–818.
- (25) Moliner, M.; Gabay, J. E.; Kliewer, C. E.; Carr, R. T.; Guzman, J.; Casty, G. L.; Serna, P.; Corma, A. Reversible Transformation of Pt Nanoparticles into Single Atoms inside High-Silica Chabazite Zeolite. J. Am. Chem. Soc. 2016, 138 (48), 15743–15750.
- (26) Fang, C.-Y.; Zhang, S.; Hu, Y.; Vasiliu, M.; Perez-Aguilar, J. E.; Conley, E. T.; Dixon, D. A.; Chen, C.-Y.; Gates, B. C. Reversible Metal Aggregation and Redispersion Driven by the Catalytic Water Gas Shift Half-Reactions: Interconversion of Single-Site Rhodium Complexes and Tetrarhodium Clusters in Zeolite HY. ACS Catal. 2019, 9 (4), 3311–3321.
- (27) Ouyang, R.; Liu, J. X.; Li, W. X. Atomistic Theory of Ostwald Ripening and Disintegration of Supported Metal Particles under Reaction Conditions. J. Am. Chem. Soc. 2013, 135 (5), 1760– 1771
- (28) Bergmann, A.; Cuenya, B. R. Operando Insights into Nanoparticle Transformations during Catalysis. ACS Catal. 2019, 9 (11), 10020–10043.
- (29) Wei, S.; Li, A.; Liu, J.-C.; Li, Z.; Chen, W.; Gong, Y.; Zhang, Q.; Cheong, W.-C.; Wang, Y.; Zheng, L. et al Direct Observation of Noble Metal Nanoparticles Transforming to Thermally Stable Single Atoms. *Nat. Nanotechnol.* 2018 139 2018, 13 (9), 856– 861
- (30) Parkinson, G. S.; Novotny, Z.; Argentero, G.; Schmid, M.; Pavelec, J.; Kosak, R.; Blaha, P.; Diebold, U. Carbon Monoxide-Induced Adatom Sintering in a Pd–Fe3O4 Model Catalyst. *Nat. Mater.* 2013 128 2013, 12 (8), 724–728.
- (31) Dessal, C.; Len, T.; Morfin, F.; Rousset, J.-L.; Aouine, M.; Afanasiev, P.; Piccolo, L. Dynamics of Single Pt Atoms on Alumina during CO Oxidation Monitored by Operando X-Ray and Infrared Spectroscopies. ACS Catal. 2019, 9 (6), 5752–5759.
- (32) Serna, P.; Rodríguez-Fernández, A.; Yacob, S.; Kliewer, C.;

- Moliner, M.; Corma, A. Single-Site vs. Cluster Catalysis in High Temperature Oxidations. *Angew. Chemie* **2021**, *133* (29), 16090–16008
- (33) Muravev, V.; Spezzati, G.; Su, Y.-Q.; Parastaev, A.; Chiang, F.-K.; Longo, A.; Escudero, C.; Kosinov, N.; Hensen, E. J. M. Interface Dynamics of Pd–CeO2 Single-Atom Catalysts during CO Oxidation. *Nat. Catal. 2021 46* **2021**, *4* (6), 469–478.
- (34) Jin, M.; Park, J. N.; Shon, J. K.; Kim, J. H.; Li, Z.; Park, Y. K.; Kim, J. M. Low Temperature CO Oxidation over Pd Catalysts Supported on Highly Ordered Mesoporous Metal Oxides. *Catal. Today* 2012, 185 (1), 183–190.
- (35) Navlani-García, M.; Miguel-García, I.; Berenguer-Murcia, Á.; Lozano-Castelló, D.; Cazorla-Amorós, D.; Yamashita, H. Pd/Zeolite-Based Catalysts for the Preferential CO Oxidation Reaction: Ion-Exchange, Si/Al and Structure Effect. Catal. Sci. Technol. 2016, 6 (8), 2623–2632.
- (36) Imbao, J.; Bokhoven, J. A. van; Nachtegaal, M. Optimization of a Heterogeneous Pd-Cu/Zeolite Y Wacker Catalyst for Ethylene Oxidation. Chem. Commun. 2020, 56 (9), 1377-1380.
- (37) Imbao, J.; van Bokhoven, J. A.; Clark, A.; Nachtegaal, M. Elucidating the Mechanism of Heterogeneous Wacker Oxidation over Pd-Cu/Zeolite Y by Transient XAS. *Nat. Commun.* 2020 111 2020, 11 (1), 1–9.
- (38) Imbao, J.; Bokhoven, J. A. van; Nachtegaal, M. On the Promotional and Inhibitory Effects of Water on Wacker-Type Ethylene Oxidation Over Pd-Cu/Zeolite Y. ACS Catal. 2021, 11 (14), 8684–8691.
- (39) Petrov, A. W.; Ferri, D.; Krumeich, F.; Nachtegaal, M.; van Bokhoven, J. A.; Kröcher, O. Stable Complete Methane Oxidation over Palladium Based Zeolite Catalysts. *Nat. Commun.* 2018 91 2018, 9 (1), 1–8.
- (40) Chen, S.; Li, S.; You, R.; Guo, Z.; Wang, F.; Li, G.; Yuan, W.; Zhu, B.; Gao, Y.; Zhang, Z. et al Elucidation of Active Sites for CH4 Catalytic Oxidation over Pd/CeO2 Via Tailoring Metal– Support Interactions. ACS Catal. 2021, 11 (9), 5666–5677.
- (41) Khivantsev, K.; Jaegers, N. R.; Kovarik, L.; Wang, M.; Hu, J. Z.; Wang, Y.; Derewinski, M. A.; Szanyi, J. The Superior Hydrothermal Stability of Pd/SSZ-39 in Low Temperature Passive NOx Adsorption (PNA) and Methane Combustion. Appl. Catal. B Environ. 2021, 280, 119449.
- (42) Tang, X.; Lou, Y.; Zhao, R.; Tang, B.; Guo, W.; Guo, Y.; Zhan, W.; Jia, Y.; Wang, L.; Dai, S.; Guo, Y. Confinement of Subnanometric PdCo Bimetallic Oxide Clusters in Zeolites for Methane Complete Oxidation. Chem. Eng. J. 2021, 418, 129398.
- (43) Li, T.; Beck, A.; Krumeich, F.; Artiglia, L.; Ghosalya, M. K.; Roger, M.; Ferri, D.; Kröcher, O.; Sushkevich, V.; Safonova, O. V. et alStable Palladium Oxide Clusters Encapsulated in Silicalite-1 for Complete Methane Oxidation. ACS Catal. 2021, 11 (12), 7371–7382.
- (44) Guo, Y.; Qi, H.; Su, Y.; Jiang, Q.; Cui, Y.-T.; Li, L.; Qiao, B. High Performance of Single-Atom Catalyst Pd1/MgO for Semi-Hydrogenation of Acetylene to Ethylene in Excess Ethylene. ChemNanoMat 2021, 7 (5), 526–529.
- (45) Zhang, L.; Zhou, M.; Wang, A.; Zhang, T. Selective Hydrogenation over Supported Metal Catalysts: From Nanoparticles to Single Atoms. Chem. Rev. 2019, 120 (2), 683– 733
- (46) Huang, W.; McCormick, J. R.; Lobo, R. F.; Chen, J. G. Selective Hydrogenation of Acetylene in the Presence of Ethylene on Zeolite-Supported Bimetallic Catalysts. J. Catal. 2007, 246 (1), 40–51.
- (47) Zhang, J.; Wang, L.; Shao, Y.; Wang, Y.; Gates, B. C.; Xiao, F.-S. A Pd@Zeolite Catalyst for Nitroarene Hydrogenation with High Product Selectivity by Sterically Controlled Adsorption in the Zeolite Micropores. *Angew. Chemie Int. Ed.* 2017, 56 (33), 9747–9751
- (48) Gu, Y.; Epling, W. S. Passive NOx Adsorber: An Overview of Catalyst Performance and Reaction Chemistry. Appl. Catal. A Gen. 2019, 570, 1–14.
- (49) Villamaina, R.; Iacobone, U.; Nova, I.; Tronconi, E.; Ruggeri, M. P.; Mantarosie, L.; Collier, J.; Thompsett, D. Mechanistic Insight in NO Trapping on Pd/Chabazite Systems for the Low-Temperature NOx Removal from Diesel Exhausts. *Appl. Catal. B Environ.* 2021, 284, 119724.
- (50) Chen, H.-Y.; Collier, J. E.; Liu, D.; Mantarosie, L.; Durán-

- Martín, D.; Novák, V.; Rajaram, R. R.; Thompsett, D. Low Temperature NO Storage of Zeolite Supported Pd for Low Temperature Diesel Engine Emission Control. *Catal. Lett.* 2016 1469 2016, 146 (9), 1706–1711.
- (51) Zheng, Y.; Kovarik, L.; Engelhard, M. H.; Wang, Y.; Wang, Y.; Gao, F.; Szanyi, J. Low-Temperature Pd/Zeolite Passive NOx Adsorbers: Structure, Performance, and Adsorption Chemistry. J. Phys. Chem. C 2017, 121 (29), 15793–15803.
- (52) Ryou, Y. S.; Lee, J.; Lee, H.; Kim, C. H.; Kim, D. H. Low Temperature NO Adsorption over Hydrothermally Aged Pd/CeO2 for Cold Start Application. *Catal. Today* 2018, 307, 93– 101.
- (53) Cui, Y.; Zhu Chen, J.; Peng, B.; Kovarik, L.; Devaraj, A.; Li, Z.; Ma, T.; Wang, Y.; Szanyi, J.; Miller, J. T. et al Onset of High Methane Combustion Rates over Supported Palladium Catalysts: From Isolated Pd Cations to PdO Nanoparticles. *JACS Au* 2021, 1 (4), 396–408.
- (54) Peterson, E. J.; DeLaRiva, A. T.; Lin, S.; Johnson, R. S.; Guo, H.; Miller, J. T.; Hun Kwak, J.; Peden, C. H. F.; Kiefer, B.; Allard, L. F. et al Low-Temperature Carbon Monoxide Oxidation Catalysed by Regenerable Atomically Dispersed Palladium on Alumina. Nat. Commun. 2014 51 2014, 5 (1), 1–11.
- (55) Li, J.; Li, M.; Li, J.; Wang, S.; Li, G.; Liu., X. Hydrodechlorination and Deep Hydrogenation on Single-Palladium-Atom-Based Heterogeneous Catalysts. Appl. Catal. B Environ. 2021, 282, 119518.
- (56) Ryou, Y. S.; Lee, J.; Kim, Y.; Hwang, S.; Lee, H.; Kim, C. H.; Kim, D. H. Effect of Reduction Treatments (H2 vs. CO) on the NO Adsorption Ability and the Physicochemical Properties of Pd/SSZ-13 Passive NOx Adsorber for Cold Start Application. Appl. Catal. A Gen. 2019, 569, 28–34.
- (57) Lee, J.; Kim, Y.; Hwang, S.; Lee, E.; Lee, H.; Kim, C. H.; Kim, D. H. Deactivation of Pd/Zeolites Passive NOx Adsorber Induced by NO and H2O: Comparative Study of Pd/ZSM-5 and Pd/SSZ-13. Catal. Today 2021, 360 (x), 350–355.
- (58) Goldsmith, B. R.; Sanderson, E. D.; Ouyang, R.; Li, W. X. CO-and NO-Induced Disintegration and Redispersion of Three-Way Catalysts Rhodium, Palladium, and Platinum: An Ab Initio Thermodynamics Study. J. Phys. Chem. C 2014, 118 (18), 9588–9597.
- (59) Paredis, K.; Ono, L. K.; Behafarid, F.; Zhang, Z.; Yang, J. C.; Frenkel, A. I.; Cuenya, B. R. Evolution of the Structure and Chemical State of Pd Nanoparticles during the in Situ Catalytic Reduction of NO with H2. J. Am. Chem. Soc. 2011, 133 (34), 13455–13464.
- (60) Newton, M. A.; Belver-Coldeira, C.; Martínez-Arias, A.; Fernández-García, M. Dynamic in Situ Observation of Rapid Size and Shape Change of Supported Pd Nanoparticles during CO/NO Cycling. Nat. Mater. 2007, 6 (7), 528–532.
- (61) Yasumura, S.; Ide, H.; Ueda, T.; Jing, Y.; Liu, C.; Kon, K.; Toyao, T.; Maeno, Z.; Shimizu, K. Transformation of Bulk Pd to Pd Cations in Small-Pore CHA Zeolites Facilitated by NO. JACS Au 2021.
- (62) Bello, E.; Margarit, V. J.; Gallego, E. M.; Schuetze, F.; Hengst, C.; Corma, A.; Moliner, M. Deactivation and Regeneration Studies on Pd-Containing Medium Pore Zeolites as Passive NOx Adsorbers (PNAs) in Cold-Start Applications. *Microporous Mesoporous Mater.* 2020, 302, 110222.
- (63) Ryou, Y. S.; Lee, J.; Cho, S. J.; Lee, H.; Kim, C. H.; Kim, D. H. Activation of Pd/SSZ-13 Catalyst by Hydrothermal Aging Treatment in Passive NO Adsorption Performance at Low Temperature for Cold Start Application. Appl. Catal. B Environ. 2017, 212, 140–149.
- (64) Ryou, Y. S.; Lee, J.; Lee, H.; Kim, C. H.; Kim, D. H. Effect of Various Activation Conditions on the Low Temperature NO Adsorption Performance of Pd/SSZ-13 Passive NOx Adsorber. Catal. Today 2019, 320, 175–180.
- (65) Pereira-Hernández, X. I.; DeLaRiva, A.; Muravev, V.; Kunwar, D.; Xiong, H.; Sudduth, B.; Engelhard, M.; Kovarik, L.; Hensen, E. J. M.; Wang, Y. et al Tuning Pt-CeO2 Interactions by High-Temperature Vapor-Phase Synthesis for Improved Reducibility of Lattice Oxygen. Nat. Commun. 2019 101 2019, 10 (1), 1–10.
- (66) Kunwar, D.; Zhou, S.; DeLaRiva, A.; Peterson, E. J.; Xiong, H.; Pereira-Hernández, X. I.; Purdy, S. C.; Veen, R. ter; Brongersma, H. H.; Miller, J. T. et al Stabilizing High Metal Loadings of

- Thermally Stable Platinum Single Atoms on an Industrial Catalyst Support. ACS Catal. 2019, 9 (5), 3978–3990.
- (67) Liu, K.; Zhao, X.; Ren, G.; Yang, T.; Ren, Y.; Lee, A. F.; Su, Y.; Pan, X.; Zhang, J.; Chen, Z. et al Strong Metal-Support Interaction Promoted Scalable Production of Thermally Stable Single-Atom Catalysts. Nat. Commun. 2020 111 2020, 11 (1), 1– 9.
- (68) Wan, Q.; Wei, F.; Wang, Y.; Wang, F.; Zhou, L.; Lin, S.; Xie, D.; Guo, H. Single Atom Detachment from Cu Clusters, and Diffusion and Trapping on CeO 2 (111): Implications in Ostwald Ripening and Atomic Redispersion. *Nanoscale* 2018, 10 (37), 17893–17901.
- (69) Li, Z.; Zhang, M.; Zhang, L.; Dong, X.; Leng, L.; Horton, J. H.; Wang, J. Engineering the Atomic Interface of Porous Ceria Nanorod with Single Palladium Atoms for Hydrodehalogenation Reaction. *Nano Res.* 2021 2021, 1–9.
- (70) Zhu, S.; Wang, H.; Wan, K.; Guo, L.-J.; He, T.; Shi, X. Water–Gas Shift Reaction on Titania-Supported Single-Metal-Atom Catalysts: The Role of Cation (Ti) and Oxygen Vacancy. J. Phys. Chem. C 2021, 125 (16), 8620–8629.
- (71) Chen, H.-Y.; Collier, J. E.; Liu, D.; Mantarosie, L.; Durán-Martín, D.; Novák, V.; Rajaram, R. R.; Thompsett, D. Low Temperature NO Storage of Zeolite Supported Pd for Low Temperature Diesel Engine Emission Control. *Catal. Letters* **2016**, *146* (9), 1706–1711.
- (72) Petrov, A. W.; Ferri, D.; Kröcher, O.; Bokhoven, J. A. van. Design of Stable Palladium-Based Zeolite Catalysts for Complete Methane Oxidation by Postsynthesis Zeolite Modification. ACS Catal. 2019, 9 (3), 2303–2312.
- (73) Losch, P.; Huang, W.; Vozniuk, O.; Goodman, E. D.; Schmidt, W.; Cargnello, M. Modular Pd/Zeolite Composites Demonstrating the Key Role of Support Hydrophobic/Hydrophilic Character in Methane Catalytic Combustion. ACS Catal. 2019, 9 (6), 4742–4753.
- (74) Ryou, Y. S.; Lee, J.; Lee, H.; Kim, C. H.; Kim, D. H. Effect of Various Activation Conditions on the Low Temperature NO Adsorption Performance of Pd/SSZ-13 Passive NOx Adsorber. Catal. Today 2017, 320, 175–180.
- (75) Wen, B.; Sun, Q.; Sachtler, W. M. H. Function of Pdn0 Cluster, Pd2+(Oxo-) Ions, and PdO Clusters in the Catalytic Reduction of NO with Methane over Pd/MFI Catalysts. J. Catal. 2001, 204 (2), 314–323
- (76) Okumura, K.; Amano, J.; Yasunobu, N.; Niwa, M. X-Ray Absorption Fine Structure Study of the Formation of the Highly Dispersed PdO over ZSM-5 and the Structural Change of Pd Induced by Adsorption of NO. J. Phys. Chem. B 2000, 104 (5), 1050–1057.
- (77) Moliner, M.; Gabay, J.; Kliewer, C.; Serna, P.; Corma, A. Trapping of Metal Atoms and Metal Clusters by Chabazite under Severe Redox Stress. ACS Catal. 2018, 8 (10), 9520–9528.
- (78) Ryou, Y. S.; Lee, J.; Kim, Y.; Hwang, S.; Lee, H.; Kim, C. H.; Kim, D. H. Effect of Reduction Treatments (H2 vs. CO) on the NO Adsorption Ability and the Physicochemical Properties of Pd/SSZ-13 Passive NOx Adsorber for Cold Start Application. Appl. Catal. A Gen. 2019, 569, 28–34.
- (79) Khivantsev, K.; Jaegers, N. R.; Koleva, I. Z.; Aleksandrov, H. A.; Kovarik, L.; Engelhard, M.; Gao, F.; Wang, Y.; Vayssilov, G. N.; Szanyi, J. Stabilization of Super Electrophilic Pd+2 Cations in Small-Pore SSZ-13 Zeolite. J. Phys. Chem. C 2019, 124 (1), 309– 321.
- (80) Bergeret, G.; Gallezot, P.; Imelik, B. X-Ray Study of the Activation, Reduction, and Reoxidation of Palladium in Y-Type Zeolites. *J. Phys. Chem.* **1981**, *85* (4), 411–416.
- (81) Van der Mynsbrugge, J.; Head-Gordon, M.; Bell, A. T. Computational Modeling Predicts the Stability of Both Pd+and Pd2+ion-Exchanged into H-CHA. J. Mater. Chem. A 2021, 9 (4), 2161–2174.
- (82) Michalik, J.; Heming, M.; Kevan, L. Trivalent and Monovalent Palladium Cations in PdNa-X Zeolite: Electron Spin Resonance and Electron Spin Echo Modulation Spectroscopic Studies. J. Phys. Chem. 1986, 90 (10), 2132–2136.
- (83) Gandhi, S. N.; Lei, G. D.; Sachtler, W. M. H. Identification of Pd3+ Ions in Zeolite L by Temperature Programmed Reduction and Electron Paramagnetic Resonance Spectroscopy. *Catal. Letters* 1993, 17 (1–2), 117–126.

- (84) Khivantsev, K.; Jaegers, N. R.; Kovarik, L.; Hanson, J. C.; Tao, F. (Feng); Tang, Y.; Zhang, X.; Koleva, I. Z.; Aleksandrov, H. A.; Vayssilov, G. N. et al Achieving Atomic Dispersion of Highly Loaded Transition Metals in Small-Pore Zeolite SSZ-13: High-Capacity and High-Efficiency Low-Temperature CO and Passive NO x Adsorbers . Angew. Chemie 2018, 130 (51), 16914–16919.
- (85) Homeyer, S. T.; Sachtler, W. M. H. Oxidative Redispersion of Palladium and Formation of PdO Particles in NaY: An Application of High Precision TPR. Appl. Catal. 1989, 54 (1), 189–202.
- (86) Gu, Y.; Zelinsky, R. P.; Chen, Y.-R.; Epling, W. S. Investigation of an Irreversible NOx Storage Degradation Mode on a Pd/BEA Passive NOx Adsorber. Appl. Catal. B Environ. 2019, 258, 118032.
- (87) Lee, J.; Kim, Y.; Hwang, S.; Lee, E.; Lee, H.; Kim, C. H.; Kim, D. H. Deactivation of Pd/Zeolites Passive NOx Adsorber Induced by NO and H2O: Comparative Study of Pd/ZSM-5 and Pd/SSZ-13. Catal. Today 2021, 360, 350–355.
- (88) Theis, J. R.; Ura, J. A. Assessment of Zeolite-Based Low Temperature NOx Adsorbers: Effect of Reductants during Multiple Sequential Cold Starts. Catal. Today 2021, 360, 340– 349.
- (89) Lardinois, T. M.; Bates, J. S.; Lippie, H. H.; Russell, C. K.; Miller, J. T.; Meyer, H. M.; Unocic, K. A.; Prikhodko, V.; Wei, X.; Lambert, C. K. et al Structural Interconversion between Agglomerated Palladium Domains and Mononuclear Pd(II) Cations in Chabazite Zeolites. *Chem. Mater.* 2021, 33 (5), 1698-1713.
- (90) Ali, A.; Chin, Y.-H.; Resasco, D. E. Redispersion of Pd on Acidic Supports and Loss of Methane Combustion Activity during the Selective Reduction of NO by CH4. Catal. Lett. 1998, 56 (2), 111–117.
- (91) Kresse, G.; Furthmüller, J. Efficient Iterative Schemes for Ab Initio Total-Energy Calculations Using a Plane-Wave Basis Set. Phys. Rev. B 1996, 54 (16), 11186.
- (92) Blöchl, P. E. Projector Augmented-Wave Method. *Phys. Rev. B* 1994, 50 (24), 17953.
- (93) Jain, A.; Ong, S. P.; Hautier, G.; Chen, W.; Richards, W. D.; Dacek, S.; Cholia, S.; Gunter, D.; Skinner, D.; Ceder, G. et al Commentary: The Materials Project: A Materials Genome Approach to Accelerating Materials Innovation. APL Mater. 2013, 1 (1), 011002.
- (94) Mandal, K.; Gu, Y.; Westendorff, K. S.; Li, S.; Pihl, J. A.; Grabow, L. C.; Epling, W. S.; Paolucci, C. Condition-Dependent Pd Speciation and NO Adsorption in Pd/Zeolites. ACS Catal. 2020, 10 (21), 12801–12818.
- (95) Perdew, J. P.; Wang, Y. Accurate and Simple Analytic Representation of the Electron-Gas Correlation Energy. *Phys. Rev. B* 1992, 45 (23), 13244.
- (96) Grimme, S.; Antony, J.; Ehrlich, S.; Krieg, H. A Consistent and Accurate Ab Initio Parametrization of Density Functional Dispersion Correction (DFT-D) for the 94 Elements H-Pu. J. Chem. Phys. 2010, 132 (15), 154104.
- (97) Grimme, S.; Ehrlich, S.; Goerigk, L. Effect of the Damping Function in Dispersion Corrected Density Functional Theory. J. Comput. Chem. 2011, 32 (7), 1456–1465.
- (98) Heyd, J.; Scuseria, G. E.; Ernzerhof, M. Hybrid Functionals Based on a Screened Coulomb Potential. J. Chem. Phys. 2003, 118 (18), 8207.
- (99) Heyd, J.; Scuseria, G. E. Efficient Hybrid Density Functional Calculations in Solids: Assessment of the Heyd–Scuseria– Ernzerhof Screened Coulomb Hybrid Functional. J. Chem. Phys. 2004, 121 (3), 1187.
- (100) Heyd, J.; Scuseria, G. E.; Ernzerhof, M. Erratum: "Hybrid Functionals Based on a Screened Coulomb Potential" [J. Chem. Phys. 118, 8207 (2003)]. J. Chem. Phys. 2006, 124 (21), 219906.
- (101) Krukau, A. V.; Vydrov, O. A.; Izmaylov, A. F.; Scuseria, G. E. Influence of the Exchange Screening Parameter on the Performance of Screened Hybrid Functionals. *J. Chem. Phys.* 2006, 125 (22), 224106.
- (102) Ong, S. P.; Richards, W. D.; Jain, A.; Hautier, G.; Kocher, M.; Cholia, S.; Gunter, D.; Chevrier, V. L.; Persson, K. A.; Ceder, G. Python Materials Genomics (Pymatgen): A Robust, Open-Source Python Library for Materials Analysis. *Comput. Mater. Sci.* 2013,

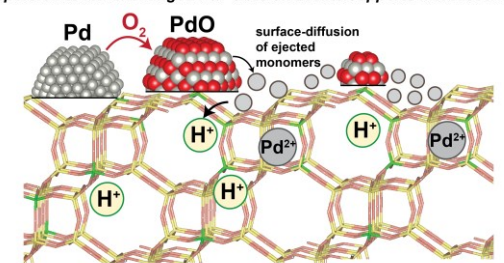
- *68*, 314–319.
- (103) Tran, R.; Xu, Z.; Radhakrishnan, B.; Winston, D.; Sun, W.; Persson, K. A.; Ong, S. P. Surface Energies of Elemental Crystals. Sci. Data 2016 31 2016, 3 (1), 1–13.
- (104) Sun, W.; Ceder, G. Efficient Creation and Convergence of Surface Slabs. Surf. Sci. 2013, 617, 53–59.
- (105) Sholl, D.; Steckel, J. A. Density Functional Theory: A Practical Introduction; Wiley, 2011.
- (106) Wulff, G. XXV. Zur Frage Der Geschwindigkeit Des Wachsthums Und Der Auflösung Der Krystallflächen. Zeitschrift für Krist. - Cryst. Mater. 1901, 34 (1–6), 449–530.
- (107) Campbell, C. T.; Mao, Z. Chemical Potential of Metal Atoms in Supported Nanoparticles: Dependence upon Particle Size and Support. ACS Catal. 2017, 7 (12), 8460–8466.
- (108) Mao, Z.; Campbell, C. T. Predicting a Key Catalyst-Performance Descriptor for Supported Metal Nanoparticles: Metal Chemical Potential. ACS Catal. 2021, 11, 8284–8291.
- (109) Hemmingson, S. L.; Campbell, C. T. Trends in Adhesion Energies of Metal Nanoparticles on Oxide Surfaces: Understanding Support Effects in Catalysis and Nanotechnology. ACS Nano 2017, 11 (2), 1196–1203.
- (110) Campbell, C. T.; Sellers, J. R. V. Enthalpies and Entropies of Adsorption on Well-Defined Oxide Surfaces: Experimental Measurements. Chem. Rev. 2013, 113 (6), 4106–4135.
- (111) Chen, M.; Schmidt, L. D. Morphology and Composition of PtPd Alloy Crystallites on SiO2 in Reactive Atmospheres. *J. Catal.* 1979, 56 (2), 198–218.
- (112) Carvill, B. T.; Lerner, B. A.; Zhang, Z. C.; Sachtler, W. M. H. Preparation of Metal/Zeolite Catalysts: Formation of Palladium Aquocomplexes in the Precursor of Palladium-Mordenite Catalysts. J. Catal. 1993, 143 (1), 314–317.
- (113) Lee, J.; Kim, J.; Kim, Y.; Hwang, S.; Lee, H.; Kim, C. H.; Kim, D. H. Improving NOx Storage and CO Oxidation Abilities of Pd/SSZ-13 by Increasing Its Hydrophobicity. *Appl. Catal. B Environ.* 2020, 277, 119190.
- (114) Chin, Y. H. C.; García-Diéguez, M.; Iglesia, E. Dynamics and Thermodynamics of Pd-PdO Phase Transitions: Effects of Pd Cluster Size and Kinetic Implications for Catalytic Methane Combustion. J. Phys. Chem. C 2016, 120 (3), 1446–1460.
- (115) Yasumura, S.; Ueda, T.; Ide, H.; Otsubo, K.; Liu, C.; Tsunoji, N.; Toyao, T.; Maeno, Z.; Shimizu, K. Local Structure and NO Adsorption/Desorption Property of Pd 2+ Cations at Different Paired Al Sites in CHA Zeolite. Phys. Chem. Chem. Phys. 2021.
- (116) Aljama, H.; Head-Gordon, M.; Bell, A.; Bell, A. T. Assessing the Stability of Pd-Exchanged Sites in Zeolites with the Aid of a High Throughput Quantum Chemistry Workkow Assessing the Stability of Pd-Exchanged Sites in Zeolites with the Aid of a High Throughput Quantum Chemistry Workflow. 2021.
- (117) Che, M.; Dutel, J. F.; Gallezot, P.; Primet, M. A Study of the Chemisorption of Nitric Oxide on PdY Zeolite. Evidence for a Room Temperature Oxidative Dissolution of Pd Crystallites. J. Phys. Chem. 1976, 80 (21), 2371–2381.
- (118) Di Iorio, J. R.; Gounder, R. Controlling the Isolation and Pairing of Aluminum in Chabazite Zeolites Using Mixtures of Organic and Inorganic Structure-Directing Agents. *Chem. Mater.* 2016, 28 (7), 2236–2247.
- (119) Ryou, Y.; Lee, J.; Cho, S. J.; Lee, H.; Kim, C. H.; Kim, D. H. Activation of Pd/SSZ-13 Catalyst by Hydrothermal Aging Treatment in Passive NO Adsorption Performance at Low Temperature for Cold Start Application. Appl. Catal. B Environ. 2017, 212, 140–149.
- (120) Li, X.; Wang, X.; Sadykov, I. I.; Palagin, D.; Safonova, O. V.; Li, J.; Beck, A.; Krumeich, F.; van Bokhoven, J. A.; Artiglia, L. Temperature and Reaction Environment Influence the Nature of Platinum Species Supported on Ceria. ACS Catal. 2021, 11 (21), 13041–13049.
- (121) Li, X.; Wang, X.; Roy, K.; Van Bokhoven, J. A.; Artiglia, L. Role of Water on the Structure of Palladium for Complete Oxidation of Methane. 2020.
- (122) Delariva, A. T.; Hansen, T. W.; Challa, S. R.; Datye, A. K. In Situ Transmission Electron Microscopy of Catalyst Sintering. J. Catal. 2013, 308, 291–305.
- (123) Castoldi, L.; Matarrese, R.; Morandi, S.; Ticali, P.; Lietti, L. Low-Temperature Pd/FER NOx Adsorbers: Operando FT-IR Spectroscopy and Performance Analysis. Catal. Today 2021,

- 360, 317-325.
- (124) Wynblatt, P.; Gjostein, N. A. Particle Growth in Model Supported Metal Catalysts—I. Theory. Acta Metall. 1976, 24 (12), 1165– 1174
- (125) Campbell, C. T.; Parker, S. C.; Starr, D. E. The Effect of Size-Dependent Nanoparticle Energetics on Catalyst Sintering. *Science* . 2002, 298 (5594), 811–814.
- (126) Dietze, E. M.; Abild-Pedersen, F.; Plessow, P. N. Comparison of Sintering by Particle Migration and Ripening through First-Principles-Based Simulations. J. Phys. Chem. C 2018, 122 (46), 26563–26569.
- (127) Yang, F.; Chen, M. S.; Goodman, D. W. Sintering of Au Particles Supported on TiO 2(110) during CO Oxidation. J. Phys. Chem. C 2009, 113 (1), 254–260.
- (128) Grillo, F.; Van Bui, H.; Moulijn, J. A.; Kreutzer, M. T.; Van Ommen, J. R. Understanding and Controlling the Aggregative Growth of Platinum Nanoparticles in Atomic Layer Deposition: An Avenue to Size Selection. *J. Phys. Chem. Lett.* **2017**, *8* (5), 975–983.
- (129) Challa, S. R.; Delariva, A. T.; Hansen, T. W.; Helveg, S.; Sehested, J.; Hansen, P. L.; Garzon, F.; Datye, A. K. Relating Rates of Catalyst Sintering to the Disappearance of Individual Nanoparticles during Ostwald Ripening. J. Am. Chem. Soc 2011, 133, 20672–20675.
- (130) Parker, S. C.; Campbell, C. T. Reactivity and Sintering Kinetics of Au/TiO2(110) Model Catalysts: Particle Size Effects. *Top. Catal.* **2007**, *44* (1–2), 3–13.
- (131) Wan, Q.; Hu, S.; Dai, J.; Chen, C.; Li, W. X. First-Principles Kinetic Study for Ostwald Ripening of Late Transition Metals on

- TiO 2 (110). J. Phys. Chem. C 2019, 123 (2), 1160-1169.
- (132) Horwath, J. P.; Voorhees, P. W.; Stach, E. A. Quantifying Competitive Degradation Processes in Supported Nanocatalyst Systems. *Nano Lett.* **2021**, *21* (12), 5324–5329.
- (133) Plessow, P. N.; Abild-Pedersen, F. Sintering of Pt Nanoparticles via Volatile PtO2: Simulation and Comparison with Experiments. *ACS Catal.* **2016**, *6* (10), 7098–7108.
- (134) Goodman, E. D.; Carlson, E. Z.; Dietze, E. M.; Tahsini, N.; Johnson, A.; Aitbekova, A.; Nguyen Taylor, T.; Plessow, P. N.; Cargnello, M. Size-Controlled Nanocrystals Reveal Spatial Dependence and Severity of Nanoparticle Coalescence and Ostwald Ripening in Sintering Phenomena. *Nanoscale* 2021, 13 (2), 930–938.
- (135) Van Den Berg, R.; Parmentier, T. E.; Elkjær, C. F.; Gommes, C. J.; Sehested, J.; Helveg, S.; De Jongh, P. E.; De Jong, K. P. Support Functionalization To Retard Ostwald Ripening in Copper Methanol Synthesis Catalysts. ACS Catal. 2015, 5 (7), 4439–4448.
- (136) Teixeira, A. R.; Chang, C. C.; Coogan, T.; Kendall, R.; Fan, W.; Dauenhauer, P. J. Dominance of Surface Barriers in Molecular Transport through Silicalite-1. J. Phys. Chem. C 2013, 117 (48), 25545–25555.
- (137) Cheung, O.; Bacsik, Z.; Fil, N.; Krokidas, P.; Wardecki, D.; Hedin, N. Selective Adsorption of CO2 on Zeolites NaK-ZK-4 with Si/Al of 1.8-2.8. ACS Omega 2020, 5 (39), 25371–25380.

TOC Graphic

Dispersion to ion-exchanged Pd2+ sites on zeolite supports increases with ...



... decreasing Pd particle size, increasing air treatment temperature, and decreasing water pressure